Materials Horizons

ROYAL SOCIETY OF CHEMISTRY

REVIEW

View Article Online
View Journal | View Issue

Check for updates

Cite this: *Mater. Horiz.*, 2025, 12, 6018

Innovative engineering strategies and mechanistic insights for enhanced carbon-based electrocatalysts in sustainable H_2O_2 production

Shun Li, *[a] Zhanpeng Zhu,[a] Yuqiao Zhang,[a] Yong Liu,[b] Xinyue Zhang*[ab] and Kwun Nam Hui*[c]

Received 5th February 2025,
Accepted 17th April 2025

DOI: 10.1039/d5mh00221d

rsc.li/materials-horizons

Hydrogen peroxide (H_2O_2) plays a crucial role in various industrial sectors and everyday applications. Given the energy-intensive nature of the current anthraquinone process for its production, the quest for cost-effective, efficient, and stable catalysts for H_2O_2 synthesis is paramount. A promising sustainable approach lies in small-scale, decentralized electrochemical methods. Carbon nanomaterials have emerged as standout candidates, offering low costs, high surface areas, excellent conductivity, and adjustable electronic properties. This review presents a thorough examination of recent strides in engineering strategies of carbon-based nanomaterials for enhanced electrochemical H_2O_2 generation. It delves into tailored microstructures (*e.g.*, 1D, 2D, porous architectures), defect/surface engineering (*e.g.*, edge sites, heteroatom doping, surface modification), and heterostructure assembly (*e.g.*, semiconductor–carbon composites, single-atom, dual-single-atom catalysts). Moreover, the review explores structure–performance interplays in these carbon electrocatalysts, drawing from advanced experimental analyses and theoretical models to unveil the mechanisms governing selective electrocatalytic H_2O_2 synthesis. Lastly, this review identifies challenges and charts future research avenues to propel carbon electrocatalysts towards greener and more effective H_2O_2 production methods.

Open Access Article. Published on 21 April 2025. Downloaded on 6/16/2026 6:54:28 AM.
This article is licensed under a Creative Commons Attribution-NonCommercial 3.0 Unported Licence.

Wider impact

The sustainable production of hydrogen peroxide (H_2O_2) is pivotal for a broad range of industrial and environmental applications, yet its current large-scale synthesis *via* the anthraquinone process remains energy-intensive and environmentally taxing. This review highlights recent advances in carbon-based electrocatalysts for decentralized, electrochemical H_2O_2 generation—a promising alternative that operates under mild conditions with minimal environmental footprint. The development of efficient, stable, and cost-effective carbon-based materials for electrochemical H_2O_2 production has profound implications for sustainable chemical manufacturing, decentralized wastewater treatment, and green energy applications. By providing a comprehensive analysis of cutting-edge catalyst engineering strategies, mechanistic insights, and structure–performance relationships, this work lays the foundation for the rational design of next-generation carbon-based electrocatalysts. Additionally, this review underscores critical challenges and future research directions, serving as a valuable roadmap for the transition toward scalable, eco-friendly H_2O_2 synthesis. The insights presented herein will not only advance fundamental scientific understanding but also accelerate practical implementation in industrial and environmental sectors.

1. Introduction

Hydrogen peroxide (H_2O_2) is an essential and environmentally friendly chemical with indispensable roles in various industrial applications, including electronics, chemical synthesis, medicine, wastewater treatment, bleaching processes, and environmental remediation.[1–4] Traditionally, industrial H_2O_2 production (~95%) is predominantly achieved through the energy-intensive anthraquinone process,[5,6] which involves complex reaction steps, requires toxic solvents under harsh conditions, and generates substantial organic waste, posing significant environmental challenges. These drawbacks have stimulated considerable interest in developing on-site, environmentally benign, energy-efficient, and cost-effective methods for H_2O_2 production, including direct synthesis using H_2 and O_2,[7,8] photocatalysis,[9–20] electrocatalysis,[21–28] mechanocatalysis,[29–32] and thermoelectrocatalysis.[33–35] Among these alternatives, electrochemical

[a] *Institute of Quantum and Sustainable Technology (IQST), School of Chemistry and Chemical Engineering, Jiangsu University, Zhenjiang, 212013, China. E-mail: shun@ujs.edu.cn*
[b] *Foshan (Southern China) Institute for New Materials, Foshan, 528200, China. E-mail: zhangxinyue@fscinm.com*
[c] *Joint Key Laboratory of the Ministry of Education, Institute of Applied Physics and Materials Engineering, University of Macau, Avenida da Universidade, Taipa, Macau SAR, China. E-mail: bizhui@um.edu.mo*

This journal is © The Royal Society of Chemistry 2025

Open Access Article. Published on 21 April 2025. Downloaded on 6/16/2026 6:54:28 AM. This article is licensed under a Creative Commons Attribution-NonCommercial 3.0 Unported Licence.

synthesis of H_2O_2 is particularly promising because it operates under mild conditions, requiring only electricity, air, and inexpensive electrolytes, while enabling high efficiency and decentralized production.[36,37] However, achieving high selectivity for the $2e^-$ reduction pathway to produce H_2O_2, instead of the $4e^-$ pathway for producing water, is critical for this process.[38,39] While noble-metal Pt- and Pd-based alloys have demonstrated excellent performance,[24,40,41] the scarcity and high cost severely limit their practical applications. Therefore, there is increasing interest in developing noble-metal-free electrocatalysts with high-efficiency and selectivity for H_2O_2 production.

Since the pioneering work on nitrogen-doped carbon nanotubes for efficient electrochemical oxygen reduction reaction (ORR) in 2009,[42] carbon-based metal-free electrocatalysts have garnered considerable research attention.[43,44] Various carbon nanomaterials, such as graphene,[45] carbon nanotubes (CNTs),[46] carbon nanofibers/wires,[47] carbon dots,[48] fullerene,[49] and porous carbon,[50] have demonstrated great potential as catalysts for electrochemical production of H_2O_2 *via* the $2e^-$ ORR pathway.[51] These materials offer great advantages like low cost, abundant availability, tunable nanostructures, excellent electrical conductivity, and adjustable electronic properties.[52,53] However, several challenges remain in optimizing these catalysts for H_2O_2 production, including (1) high overpotential, low catalytic activity and selectivity compared to precious metal catalysts; (2) unclear mechanisms involving active sites and reaction pathways; (3) poor stability and durability in acidic or alkaline environments; (4) difficulty of integration with electrochemical systems for scalable production.

To overcome these inherent limitations, many strategies have been developed in the past few decades. Several important review papers have been published on carbon-based nanomaterials for H_2O_2 production.[53–57] As a rapidly growing field, recent studies have demonstrated notable advancements in the rational design and fabrication of carbon-based electrocatalysts. Moving beyond traditional catalyst optimization methods, innovative engineering strategies have been developed, such as precise modulation of microstructures (*e.g.*, programed hierarchical structure), multi-component synergistic engineering (*e.g.*, topological and doping effect), and the incorporation of atomically precise catalytic centers (*e.g.*, dual-single-atom sites). These modification strategies have led to significantly enhanced H_2O_2 production activity, selectivity and stability, achieving performance levels that rival or even surpass those of the leading catalysts reported to date. Therefore, it is timely to provide a comprehensive overview of the latest breakthroughs in advanced engineering strategies for carbon-based nanomaterials in electrochemical H_2O_2 production (Fig. 1). First, we describe the mechanisms of the $2e^-$ ORR and water oxidation reaction (WOR) pathways and elucidate the key factors influencing selectivity and activity. Next, we thoroughly summarize the recent progress in carbon-based electrocatalysts for H_2O_2 synthesis, emphasizing their underlying structure–performance relationships, particularly in the $2e^-$ ORR pathway. Finally, we highlight the current

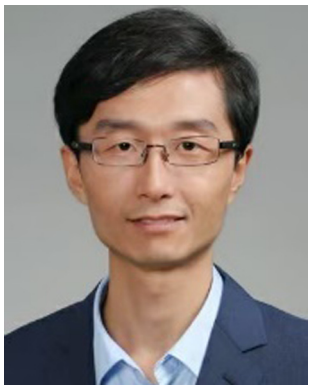

Shun Li

Dr Shun Li is Jinshan distinguished professor at Jiangsu University in China. He obtained his PhD Degree at Institut national de la recherche scientifique (INRS), Canada in 2015. He worked as a Research Assistant Professor at Southern University of Science and Technology, China. He was recognized among the top 2% of scientists globally by Stanford University/Elsevier in 2024. His research interests are focused on harvesting thermal/mechanical energy for diverse catalytic applications.

Xinyue Zhang

Xinyue Zhang received her PhD degree at the Northeastern University in China in 2022. Her research interests include the synthesis of advanced nanomaterials and their application in the field of catalysis/advanced oxidation/environmental remediation.

Kwun Nam Hui

Dr Kwun Nam Hui is an associate professor at the Institute of Applied Physics and Materials Engineering at the University of Macau and a Fellow of the Royal Society of Chemistry. Since 2021, Dr Hui has also been recognized among the top 2% of scientists globally by Stanford University/Elsevier. He obtained his PhD in Electrical and Electronic Engineering from the University of Hong Kong in 2009. Following the completion of his doctorate, he pursued a postdoctoral research position at Rutgers, the State University of New Jersey, in the Department of Electrical and Computer Engineering. His recent research focuses on innovative energy materials and devices.

Open Access Article. Published on 21 April 2025. Downloaded on 6/16/2026 6:54:28 AM. This article is licensed under a Creative Commons Attribution-NonCommercial 3.0 Unported Licence.

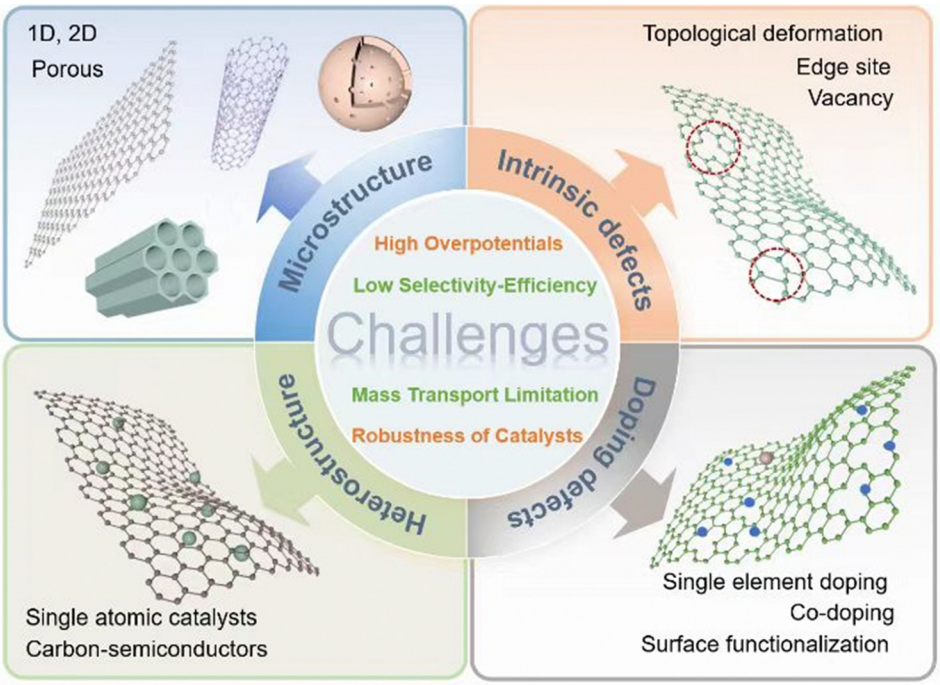

Fig. 1 Schematics of key challenges and corresponding modification strategies of carbon-based electrocatalysts for H_2O_2 production.

challenges and propose future directions for the rational design and large-scale utilization of advanced carbon-based electrocatalytic materials.

2. Fundamentals of electrochemical H_2O_2 production

Electrocatalytic H_2O_2 production can be achieved through both the ORR and WOR (Fig. 2). These processes involve multi-electron reactions characterized by several elementary steps and potential intermediates (*e.g.*, *OOH and *OH).[58] The mechanisms of the ORR and WOR reactions are presented below in detail.

2.1. Two-electron pathway *via* the oxygen reduction reaction (ORR)

Generally, the ORR involves a complex multi-electron transfer process, which can be categorized as dissociative and associative mechanisms. For the dissociative mechanism, the O–O bond in the adsorbed O_2 cleaves directly, resulting in the formation of O_{ads} and H_2O as the final product. In contrast, the associative mechanism involves the couple of adsorbed O_2 with an electron (e^-) and a proton (H^+) to form the *OOH intermediate,[59] which can further accept another e^- and H^+ to produce H_2O_2. Additionally, the O–O bond in the *OOH intermediate may also dissociate, yielding O_{ads} and OH_{ads} and ultimately leading to the formation of H_2O (*OOH + H^+ + e^- → *O + H_2O).[60] Thus, H_2O_2 is obtained as the main product by intervening in the dissociation of the peroxide species from the surface, as shown in eqn (1) and (2).[61,62] Thus, the two competitive reactions involving the *OOH intermediate determine the selectivity for H_2O_2 generation.

$$O_2 + * + H^+ + e^- \rightarrow *OOH \quad (1)$$

$$*OOH + H^+ + e^- \rightarrow H_2O_2 + * \quad (2)$$

Consequently, ORR mechanisms can be divided into two pathways: the $2e^-$ or $4e^-$ pathway. The $4e^-$ pathway is preferred as the cathode reaction in fuel cells and metal–air batteries to obtain higher voltage and energy efficiency, while the electrochemical production of H_2O_2 relies on the $2e^-$ pathway (eqn (3) and (4)).

In acidic medium:

$$O_2 + 2H^+ + 2e^- \rightarrow H_2O_2 \quad (E^0 = 0.67\ V_{RHE}) \quad (3)$$

In alkaline medium (pH > 11.6):

$$O_2 + H_2O + 2e^- \rightarrow HO_2^- + OH^- \quad (E^0 = 0.76\ V_{RHE}) \quad (4)$$

A critical aspect in determining the pathway of the ORR is the adsorption mode of O_2 molecules on the catalyst's surface. In particular, when O_2 is adsorbed in the Pauling mode, the O–O bond is less likely to break, thus favoring H_2O_2 generation.[63]

2.2. Two-electron pathway *via* the water oxidation reaction (WOR)

The WOR process can occur through $1e^-$, $2e^-$, and $4e^-$ oxidative pathways and H_2O_2 can be generated *via* the $2e^-$ pathway, while the complete oxidation pathway to O_2 needs to be avoided.[64–66] The specific WOR steps by the $2e^-$ pathway for H_2O_2 production are as follows:

$$2H_2O \rightarrow H_2O_2 + 2H^+ + 2e^- \quad (E^0 = 1.76\ V_{RHE}) \quad (5)$$

$$* + H_2O \rightarrow *OH + H^+ + e^- \quad (6)$$

 This journal is © The Royal Society of Chemistry 2025

Open Access Article. Published on 21 April 2025. Downloaded on 6/16/2026 6:54:28 AM.
This article is licensed under a Creative Commons Attribution-NonCommercial 3.0 Unported Licence.

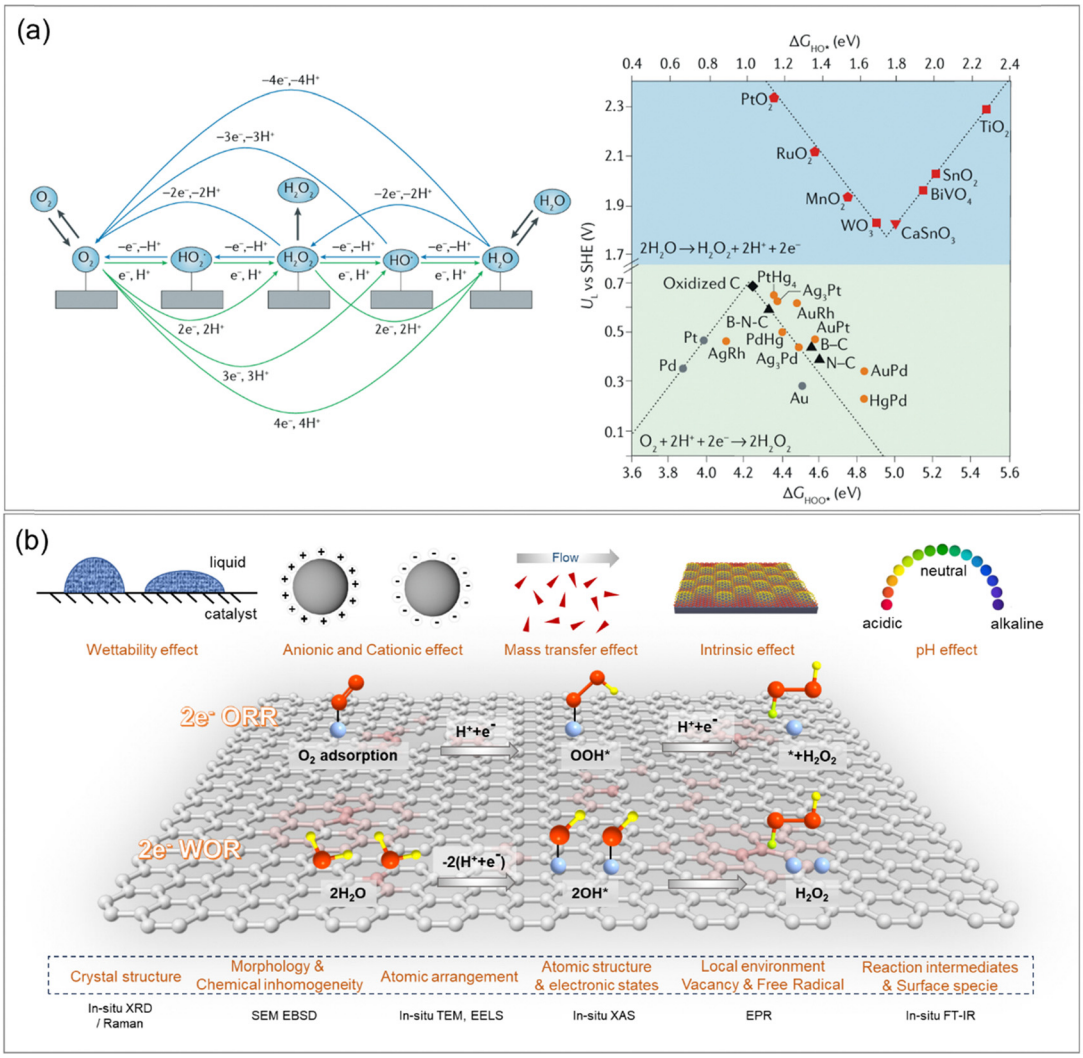

Fig. 2 (a) Possible reduction pathways of the ORR and WOR for electrocatalysis H_2O_2 production (left) and a plot of theoretical limiting potential (U_L) against Gibbs free energies of binding *OOH (ΔG_{HOO*}) and *OH (ΔG_{HO*}) for H_2O_2 electrosynthesis (right) of different types of electrocatalysts. U_L is the least positive (anodic) or negative (cathodic) potential at which both electron transfers are downhill in free energy.[2] Copyright 2019, Nature Publishing Group. (b) Schematic illustration of crucial factors and characterization techniques for investigating the electrocatalytic mechanism.

$$*OH + *OH \rightarrow H_2O_2 \quad (7)$$

The key issue for determining the pathway of the WOR is the recombination of *OH species on the catalyst's surface. Specifically, if *OH is not further oxidized to *O or •OH, H_2O_2 generation is favored.

2.3. Mechanistic insights into electrochemical H_2O_2 production

In the electrocatalytic production of H_2O_2 *via* the ORR and WOR mechanisms, the key factors determining the efficiency and selectivity mainly include catalyst materials and electrolyte properties. Catalysts with optimized surface electronic structures, such as those exhibiting moderate adsorption energies for oxygen intermediates (*e.g.*, *OOH), favor the $2e^-$ pathway with low overpotential. Additionally, surface properties like porosity, defects, and functional groups can enhance the accessibility of active sites and improve mass transport, further boosting H_2O_2 production. In addition, the electrolyte (*e.g.*, ion type, pH value) also plays a critical role in tuning the reaction kinetics and selectivity. Overall, achieving high activity and selectivity in H_2O_2 electrocatalysis requires a balance modulation of these factors.

The electrochemical synthesis of H_2O_2 using carbon-based electrocatalysts involves complex reaction mechanisms that govern their performance in terms of activity, selectivity, and stability. Density functional theory (DFT) calculations (Fig. 2a) reveal that certain defect configurations in carbon-based materials appear at the pinnacle of the $2e^-$ ORR volcano plot,[2] highlighting their role as highly active sites. Based on the fundamental mechanisms, key engineering strategies are categorized into: (1) modulation of materials'surface that governs selectivity and mass transfer, (2) reaction pathways and intermediates, and (3) selection of the electrolyte. This section provides a cohesive framework for understanding the underlying principles of

Open Access Article. Published on 21 April 2025. Downloaded on 6/16/2026 6:54:28 AM. This article is licensed under a Creative Commons Attribution-NonCommercial 3.0 Unported Licence.

electrocatalysis H_2O_2 production (Fig. 2b), which is crucial for optimizing the reactant adsorption/activation, stabilization of intermediates, and efficient product release.

2.3.1. Surface properties of electrocatalysts. The surface properties of electrocatalysts, where charge and mass transfer of electrochemical reaction occurs, have a crucial effect on the reaction activity.[67] The surface electronic structure of the electrocatalyst directly determines the adsorption behavior of oxygen-bearing intermediates (O*, OH*, and OOH*), thereby influencing the activity and selectivity of both the $2e^-$ ORR and WOR. For instance, defect engineering (*e.g.*, edge sites, topological defects, curvature effects, and doping) modulates surface electronic structures and creates active sites to stabilize *OOH and activate O_2, leading to reduced reaction barriers and favoring the formation of H_2O_2. In addition, introducing single-atom catalysts on the surface of carbon materials provides precise control over adsorption and binding energies. Microstructure tailoring, such as designing mesoporous hollow nanoreactors, can enhance mass transport and intermediate retention by facilitating O_2 enrichment and H_2O_2 diffusion.

Moreover, the wettability of the reaction interface, especially hydrophilicity/hydrophobicity, plays an important role in regulating the adsorption/desorption dynamics of products on the electrode surface.[68] For instance, hydrophilic surfaces may facilitate ion transport and reduce gas bubbles overpotential, while controlled hydrophobicity can promote O_2 diffusion to active sites, a crucial factor for the ORR. The balance between hydrophilic and hydrophobic domains can be optimized through chemical functionalization or micro/nanostructuring to create ideal triple-phase boundaries for simultaneous O_2 supply and H_2O_2 release.[69–71] When combined with other catalyst modifications (defect engineering, heteroatom doping, *etc.*), wettability control creates synergistic effects that enhance both the kinetics and thermodynamics of the $2e^-$ pathways, bridging fundamental mechanistic understanding with practical catalyst optimization for efficient H_2O_2 production.

2.3.2. Reaction pathways and intermediates. Both the $2e^-$ ORR and WOR pathways enable selective H_2O_2 production, yet they proceed through fundamentally different reaction mechanisms involving critical intermediates. Theoretical studies have established that the binding energies of ΔG_{OOH^*} and ΔG_{OH^*} serve as main descriptors for catalysts to favour H_2O_2 formation from O_2 or H_2O, respectively.

Based on the ORR mechanism, three factors are crucial to ensure high H_2O_2 production selectivity.[72,73] Firstly, a suitable O_2 adsorption model is necessary to prevent the dissociative pathway. When the adsorption state is in Pauling mode, the O–O bond is unlikely to break, which is favorable for the generation of H_2O_2. Secondly, the catalysts should balance the strong adsorption of O_2 to facilitate OOH* generation, while allowing moderate desorption to produce H_2O_2 rather than H_2O. Thirdly, it is important to ensure rapid release of the produced H_2O_2 from the catalyst surface to avoid further reduction or decomposition.

As for the WOR process, the selectivity among the $1e^-$, $2e^-$, and $4e^-$ pathways is determined using the descriptors ΔG_{*OH} and ΔG_{*O}, where $\Delta G_{*O} - 2\Delta G_{*OH} = 0.28$ eV.[74,75] The selectivity of H_2O_2 production depends on the recombination of two *OH intermediates; If *OH is further oxidized to *O or •OH, the H_2O_2 formation is suppressed. At $\Delta G_{*OH} = 2.38$ eV, *OH can form either H_2O_2 or *O. If the adsorption energy of *O exceeds the production energy of H_2O_2 (3.52 eV), the reaction favors the $4e^-$ pathway (with $\Delta G_{*O} < 3.52$ eV and $\Delta G_{*OH} < 1.62$ eV). The optimal condition for the target $2e^-$ WOR occurs when ΔG_{*OH} is between 1.62 and 2.38 eV, as the standard potential is more positive than that of H_2O_2 oxidation ($E^0 = 0.67$ V_{RHE}).

2.3.3. Role of the electrolyte. The electrolyte also plays an important role in the electrochemical H_2O_2 production process, particularly when pairing the $2e^-$ ORR and $2e^-$ WOR in traditional liquid electrolytes ranging from acidic to alkaline pH. For the $2e^-$ ORR, the pH of the electrolyte affects the selectivity due to the solvation effects and surface adsorbed species (such as $*OH_{ads}$ and anions).[22,76] In alkaline medium, the •OH species are strongly adsorbed on the catalyst surface, facilitating outer-sphere electron transfer *via* water-solvated molecular O_2. In contrast, acidic electrolytes promote high proton mobility, resulting in low concentrations of adsorbed •OH species. Here, O_2 molecules are chemisorbed on the catalyst surface, receiving electrons through the inner-Helmholtz plane (IHP) process.[77]

3. Engineering strategies for carbon-based electrocatalysts

The catalytic performance of materials is intrinsically determined by the physicochemical properties of their surfaces, which govern the adsorption and desorption of reactive species and influence key parameters such as activity, selectivity, and stability. Pristine carbon materials often suffer from low catalytic activity and poor selectivity due to their relatively inert surfaces and limited active sites. To overcome these inherent limitations, a range of advanced engineering strategies have been developed, including microstructure design, defect engineering, chemical doping, surface functionalization, and introduction of heterojunction or atomic sites, to enhance the electrocatalytic performance of carbon nano-catalysts toward H_2O_2 production, primarily focusing on the $2e^-$ ORR pathway. The roadmap of carbon-based electrocatalysts illustrating the key findings is summarized in Fig. 3.

3.1. Microstructure tailoring

Modifying the microstructure of carbon materials plays a vital role in boosting their catalytic performance. Constructing various nanostructures, such as 1D (*e.g.*, nanotubes and nanorods), 2D (*e.g.*, graphene), porous architectures (*e.g.*, macropores, mesopores and micropores), and hierarchical structures, leads to significant improvements in surface area, exposure of active sites, mass diffusion, and electrical conductivity. These enhanced properties are crucial for increasing the efficiency and selectivity of the catalyst during the electrocatalysis process.

The catalytic performance of microstructures is heavily influenced by their dimensions and porosity, as these factors determine the accessibility of active sites and the transport of

 This journal is © The Royal Society of Chemistry 2025

Open Access Article. Published on 21 April 2025. Downloaded on 6/16/2026 6:54:28 AM.
This article is licensed under a Creative Commons Attribution-NonCommercial 3.0 Unported Licence.

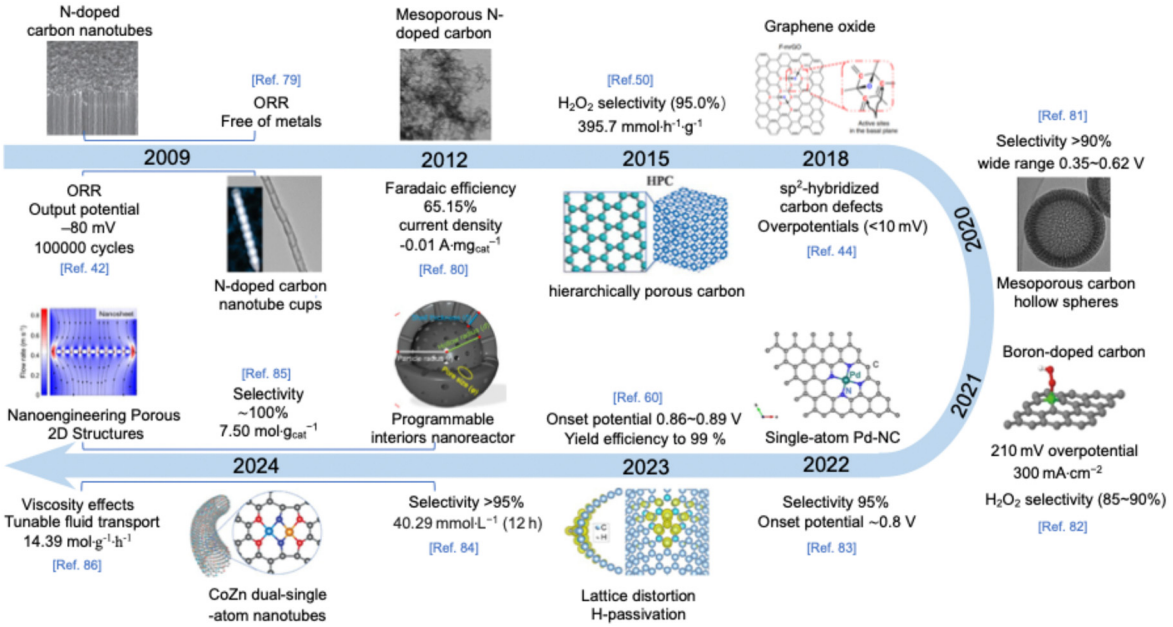

Fig. 3 Timeline of engineering strategies for carbon-based electrocatalysts for H_2O_2 production: N-doped carbon nanotubes,[42] reduced graphene oxide,[44] hierarchically porous carbon,[50] N-doped carbon nanotube cups,[78] mesoporous N-doped carbon,[79] mesoporous carbon hollow spheres,[80] boron-doped carbon,[81] single-atom Pd/carbon,[82] lattice distortion carbon,[59] mesoporous carbon spheres,[83] CoZn dual-single-atom carbon nanotubes,[84] and porous 2D structures.[85]

reactants and products.[86,87] For example, 1D nanostructures such as nanotubes provide excellent electron transport pathways, while 2D nanostructures like graphene sheets offer high surface areas for active site exposure. Moreover, when porous architectures are introduced, such as macropores (larger pores that facilitate mass transport), mesopores (intermediate-sized pores that enhance exposure of active sites), and micropores (smaller pores that control the retention of reactants), the material's ability to regulate reaction intermediates and diffusion kinetics can be greatly promoted.[88] Moreover, the 2e$^-$ ORR can be regulated by controllable pore structures through adjusting the coordination of reaction intermediates. By optimizing the exposure of active sites and retention time of H_2O_2 within specialized pore sizes, the overall performance of the catalyst can be finely tuned.[51,89] Recently, hollow structures that typically feature lower density and larger surface area have garnered significant attention due to their unique properties compared to solid counterparts, by facilitating mass transport and enhancing the availability of active sites. The increased surface-to-volume ratio in hollow structures further contributes to higher utilization of the catalyst material, making them highly attractive for electrocatalytic H_2O_2 production.[80,90–92] This section will mainly focus on the key latest advances in the rational design of high efficient carbon-based electrocatalysts with controllable microstructures.

Precision nanoengineering of porous 2D structures has been emerging as a promising strategy for fine-tuning catalytic reactions. Guided by finite element simulation (FEM), Tian *et al.*[85] designed and fabricated porous 2D carbon nanomaterials by introducing mesopores with diameters of 5–10 nm to facilitate fluid acceleration (Fig. 4a–c). The resulting mesoporous carbon nanosheets exhibited exceptional electrocatalytic H_2O_2 production performance, achieving a high selectivity of >95% and a diffusion-limiting disk current density of −3.1 mA cm^{-2} (Fig. 4d–f). FEM simulations revealed that the mesoporous nanosheet significantly accelerated fluid flow within the meso-channels due to viscosity effects and the constricted flow path (Fig. 4g), validating the crucial role of mesoporous 2D structures in enhancing local diffusion. Remarkably, the electrolysis process in a flow cell achieved a high production rate of 14 390 mmol g^{-1} h^{-1}, yielding a medical-grade H_2O_2 solution. This work demonstrates an effective approach to improving the activity and selectivity of porous carbon materials by influencing local fluid transport behavior.

Mesoporous hollow nanoreactors (MHNs), a novel class of rationally designed catalytic material, offer unique advantages of complex catalytic processes due to their hollow internal spaces and mesoporous structures.[93–95] The mesoporous channels can create a confined microenvironment that enhances molecular diffusion, adsorption and surface reactions, enabling tunable catalytic pathways. For instance, Tian *et al.*[83] demonstrated precisely engineered carbon spheres by integrating micromechanics with controllable synthesis to improve their 2e$^-$ ORR catalytic activity (Fig. 5). The mesoporous channels accelerated the fluid flow and facilitated the transport of generated H_2O_2 into the solution (Fig. 5a–c), thereby minimizing electro-reduction on the catalysts' surface. Increased flow rates led to O_2 enrichment in the pore channels (Fig. 5d), while the accumulation of OH$^-$ ions (Fig. 5e) elevated the local pH within the MHNs. And the surface of the $MHCS_{0.5}$ electrode demonstrated the highest OH$^-$ concentrations among all samples (Fig. 5f). As a result, $MHCS_{0.5}$ exhibited exceptional 2e$^-$ ORR performance under neutral electrolyte conditions (pH = 7),

Open Access Article. Published on 21 April 2025. Downloaded on 6/16/2026 6:54:28 AM.
This article is licensed under a Creative Commons Attribution-NonCommercial 3.0 Unported Licence.

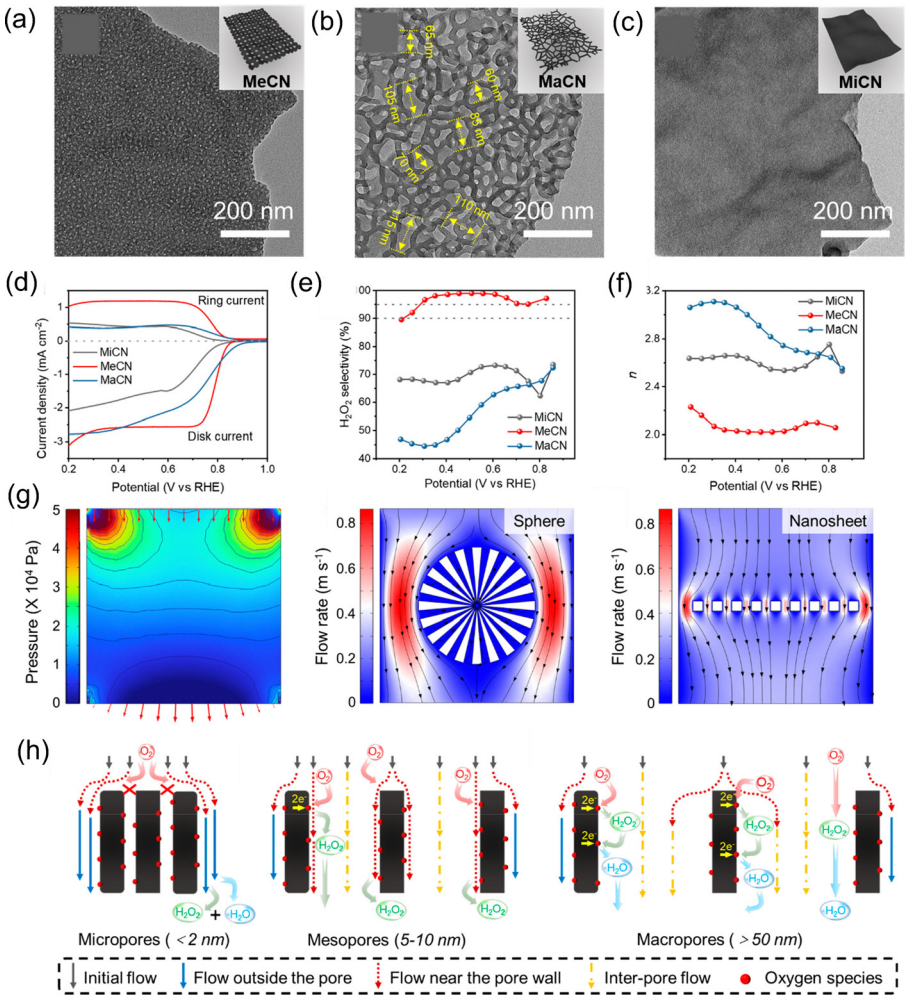

Fig. 4 Nanoengineering of porous 2D carbon structures for ORR H_2O_2 production. TEM images and structural models of (a) MeCN, (b) MaCN, and (c) MiCN; (d) LSV curves recorded in an O_2-saturated KOH, (e) calculated H_2O_2 selectivity, and (f) ORR electron transfer number at various potentials; (g) color mapping of the spatial pressure distribution, and spatial distribution of flow velocities of the mesoporous carbon sphere and nanosheet model (pore size: 5 nm); (h) proposed fluid behavior and ORR processes in micropores, mesopores, and macropores. Reproduced with permission from ref. 85. Copyright 2024, the American Chemical Society.

with a diffusion-limited disk current of $-2.8\,mA\,cm^{-2}$ at 0.2 V, an onset potential of 0.6 V (*vs.* RHE), and an H_2O_2 selectivity exceeding 85%, outperforming most carbon-based catalysts reported in the literature.

3.2. Defect engineering

Defects in carbon nanomaterials, such as vacancies, rings, edge sites, topological defects, and lattice distortion, play a crucial role in modulating their electronic structure and surface chemistry. Introducing structural defects can generate abundant active sites that enhance the adsorption and activation of oxygen molecules, thereby improving the selectivity and efficiency of the ORR towards H_2O_2 production.[96,97] For instance, vacancies provide more exposed active sites, while edge defects create abundant unsaturated bonds.[98] Beyond enhancing catalytic reactivity, defect engineering could also improve the durability and stability of the electrochemical system, making it more suitable for industrial applications.[96] In the past decade, significant efforts have been made to explore defective carbon catalysts for electrochemical H_2O_2 production.[99–102] In this section, we will highlight the key advances in defect engineering of the carbon electrocatalyst including both intrinsic defects (*e.g.*, edge defects, topological defects) and chemical doping with heteroatoms (*e.g.*, single element and dual-element doping).

3.2.1. Intrinsic defects. Edge engineering has emerged as a promising strategy to activate inert carbon surfaces and modify their local electronic structure by introducing unpaired electrons.[103,104] For example, Jing *et al.*[98] developed an organic–inorganic hybrid co-assembly approach to fabricate mesoporous carbon nanofibers (MCNFs) with tunable edge site densities and pore sizes, using ammonia to catalyze the modular molding of SiO_2 and resin (Fig. 6a). They demonstrate that the density of carbon edge sites can be controlled to enhance ORR activity and selectivity. The optimized MCNF catalyst exhibited outstanding $2e^-$ ORR performance (Fig. 6b and c), achieving high H_2O_2 selectivity (>90%) over a wide potential range of 0.6 V, along with a large cathodic current

 This journal is © The Royal Society of Chemistry 2025

Open Access Article. Published on 21 April 2025. Downloaded on 6/16/2026 6:54:28 AM.
This article is licensed under a Creative Commons Attribution-NonCommercial 3.0 Unported Licence.

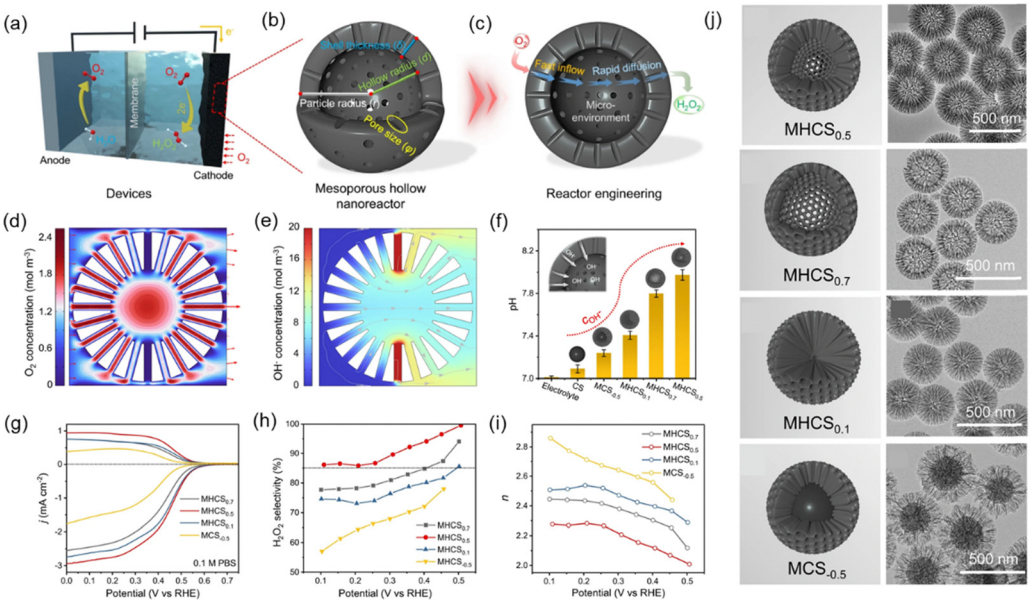

Fig. 5 Nanoreactor design based on carbon nanospheres. (a)–(c) Schematic diagram of the electrochemical 2e$^-$ ORR to produce H_2O_2 over the designed nanoreactor; Spatial distribution of (d) O_2 and (e) OH^- concentration in the mesoporous carbon sphere model; (f) OH^- concentrations on the surface of $MHCS_x$; (g) LSV curves of RRDE measurements, (h) H_2O_2 selectivity, and (i) electron transfer number at various applied potentials; (j) structural model and TEM images of $MHCS_x$. Reproduced with permission from ref. 83. Copyright 2024, Nature Publishing Group.

density of −3.0 mA cm^{-2} at 0.2 V *vs.* RHE. As illustrated in Fig. 6d, the defect configurations comprised vacancies (VD1 and VD2), topological defects (TD3), and edge defects, including zigzag and armchair types (ZD4 and AD5, respectively). The introduction of these defects enhanced *OOH adsorption, with the zigzag defect (ZD4) and armchair (AD5) defects exhibiting free energies of 3.67 and 3.62 eV, respectively, values close to the ideal standard free energy of 3.52 eV (Fig. 6e and f). These results demonstrate that edge defects can effectively promote the 2e$^-$ ORR pathway, offering a promising route to achieving high H_2O_2 production activity selectivity in carbon-based electrocatalysts.

By introducing asymmetric structures into a hexagonal carbon lattice, the symmetry can be broken to allow rapid electron transfer, thus promoting the electrocatalytic process. Recently, topological defects have been recognized as effective active sites toward catalyzing different electrochemical reactions. She *et al.*[105] investigated the curvature-dependent ORR

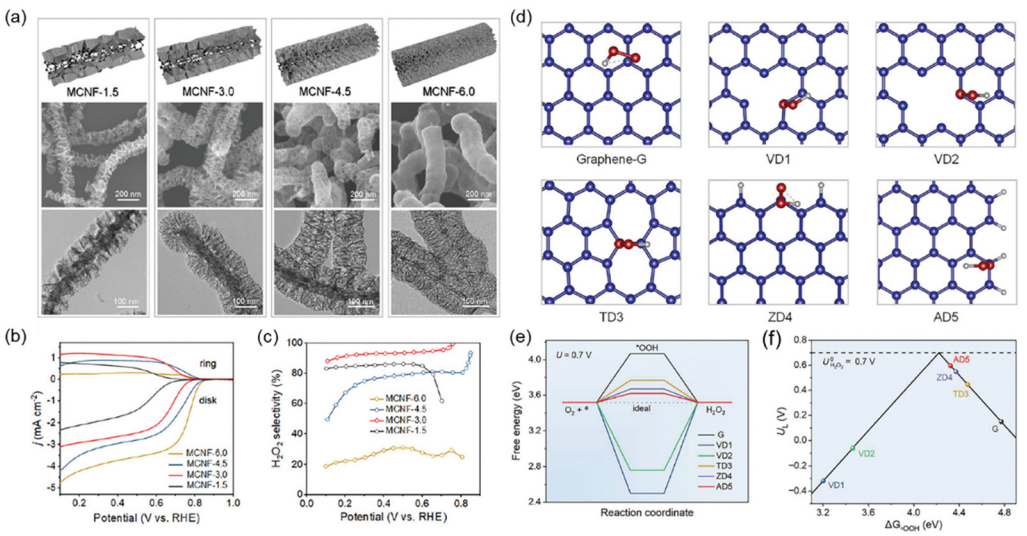

Fig. 6 Edge defect engineering of ORR activity. (a) Schematic, SEM, and TEM images of different mesoporous carbon nanofibers (MCNFs); (b) LSV curves and (c) calculated H_2O_2 selectivity; (d) preferred *OOH adsorption configurations on pristine graphene and different carbon defects models (blue, grey, and red represent C, H, and O atoms, respectively); (e) free-energy profiles of ORR paths at a potential of 0.7 V; (f) volcano plot for the most active structures, with the limiting potential depicted as a function of ΔG_{*OOH}. Reproduced with permission from ref. 98. Copyright 2023, Wiley-VCH.

Open Access Article. Published on 21 April 2025. Downloaded on 6/16/2026 6:54:28 AM.
This article is licensed under a Creative Commons Attribution-NonCommercial 3.0 Unported Licence.

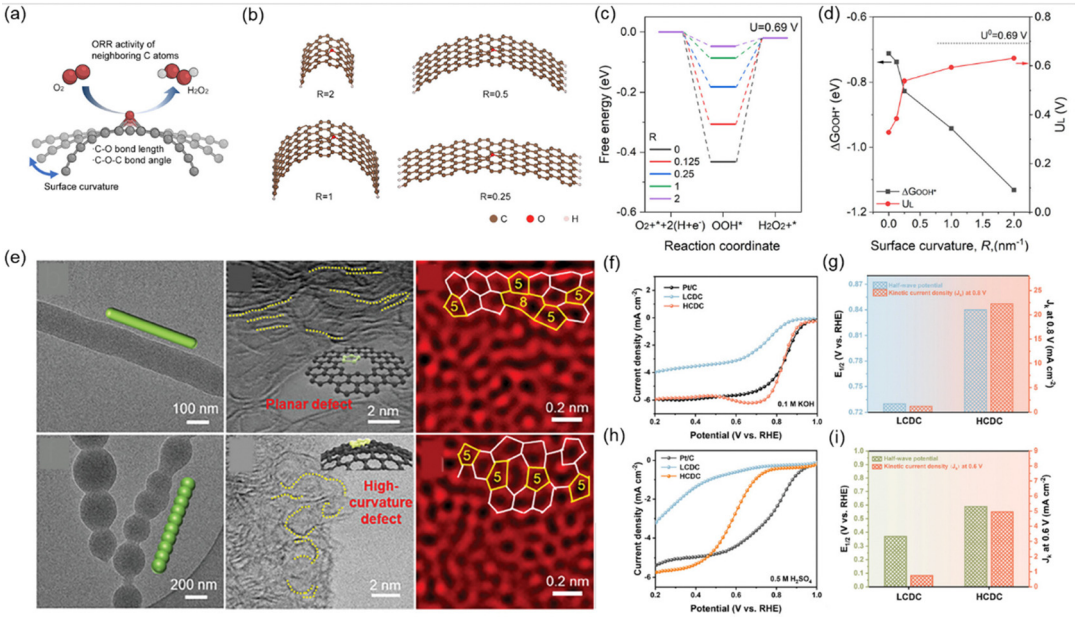

Fig. 7 Investigation of the curvature-dependent ORR activity. (a) Schematic illustration of the epoxy group grafted on the curvature varied carbon surface and (b) geometry optimized atomic models of different R values; (c) calculated ORR free energy diagrams at 0.69 V and (d) correlations between ΔG_{OOH^*} and U_L to surface curvature. Reproduced with permission from ref. 105. Copyright 2024, the American Chemical Society. (e) TEM, HRTRM, and AC HAADF-STEM images of LCDC and HCDC (insets show the morphology and atomic structure diagrams); (f) LSV curves in O_2-saturated KOH and (g) comparison of J_k (0.8 V) and $E_{1/2}$; (h) LSV curves of LCDC, HCDC, and Pt/C in O_2-saturated H_2SO_4 and (i) comparison of J_k (0.6 V) and $E_{1/2}$. Reproduced with permission from ref. 106. Copyright 2024, Wiley-VCH.

activity of surface oxidized carbon nanotubes (o-CNTs) (Fig. 7a–d). Computation modeling suggested that the curvature can alter the epoxy group geometry, exerting greater strain on the C–O bond in smaller diameter o-CNTs that leads to improved activity. Increase of R results in stronger OOH* binding and a lower ΔG_{OOH^*} (Fig. 7c), and 2e-ORR theoretical potential (U_L) approaches the equilibrium potential ($E^0 = 0.69$ V) on a model with a greater R (Fig. 7d). As predicted, the o-CNT with the smallest diameter ($\sim$8 nm) exhibited the highest faradaic efficiency $>$85% and a mass activity of 161 A g^{-1} at 0.65 V. Very recently, Wang *et al.*[106] fabricated carbon nanomaterials with rich topological defect sites and curved defective surface by controlling the pyrolytic shrinkage process of precursors (Fig. 7e–i). Theoretical calculations demonstrated that bending the defect sites can manipulate the local electronic structure, facilitate the charge transfer to key intermediates, and reduce the ORR energy barrier. Experimental results showed that a large kinetic current density of 22.5 mA cm^{-2} at 0.8 V *vs.* RHE was obtained for high-curvature defective carbon (HCDC), which is $\sim$18 times of low-curvature defective carbon (LCDC). Further increasing the defect densities of HCDC results in a dual-regulated product (HCHDC), which exhibited exceptional ORR activity in both alkaline and acidic media (half-wave potentials of 0.88 and 0.74 V, respectively), exceeding most of the reported carbon electrocatalysts. These studies highlight the crucial role of curvature effect in promoting electrocatalytic activity and offer new guidance to the design of advanced carbon nano-catalysts for H_2O_2 production.

3.2.2. Heteroatom doping. Incorporating non-metallic/metallic heteroatoms, such as boron (B),[107–109] nitrogen (N),[102,110] oxygen (O),[111,112] fluorine (F),[111] and sulfur (S),[113] into the carbon lattice can disturb the electron symmetry in the aromatic carbon networks, leading to inhomogeneous compositions and the formation of active sites by tailoring the charge and spin densities of carbon atoms. In addition, heteroatoms could introduce active functional groups (oxygen-bearing functional groups) onto the carbon matrix, which can serve as active sites for the $2e^-$ ORR, to achieve high electrocatalytic activity. Although extensive studies have been reported on this strategy, herein we only summarize the latest achievements on heteroatom doping to enhance electrocatalytic H_2O_2 generation activity.

In 2021, Xia *et al.*[81] reported a boron-doped carbon (B–C) catalyst (Fig. 8). Compared to the state-of-the-art oxidized carbon catalyst, the B–C catalyst presented significantly lowered overpotential by 210 mV under industrial-level currents (300 mA cm^{-2}) while maintaining high H_2O_2 selectivity (85–90%) (Fig. 8e and f). DFT calculations revealed that the boron dopant site is responsible for high H_2O_2 activity and selectivity due to the reduced thermodynamic and kinetic reaction barriers (Fig. 8c and d). Integrated in a porous solid electrolyte reactor, the B–C catalyst demonstrated continuous generation of pure H_2O_2 solutions with high current density ($\sim$400 mA cm^{-2}) and selectivity ($\sim$95%), presenting their great potential for practical applications in the future.

Oxygen-doped carbon quantum dots (o-CQDs) with C–O–C surface functional groups were fabricated with tunable electronic structures by varying isomerization precursors,[112] presenting a remarkable H_2O_2 selectivity of 96.2% ($n = 2.07$) at 0.68 V *vs.* RHE along with a low Tafel slope of 66.95 mV dec^{-1}, and maintaining consistent production stability of H_2O_2 over 120 h. In addition, a

 This journal is © The Royal Society of Chemistry 2025

Open Access Article. Published on 21 April 2025. Downloaded on 6/16/2026 6:54:28 AM. This article is licensed under a Creative Commons Attribution-NonCommercial 3.0 Unported Licence.

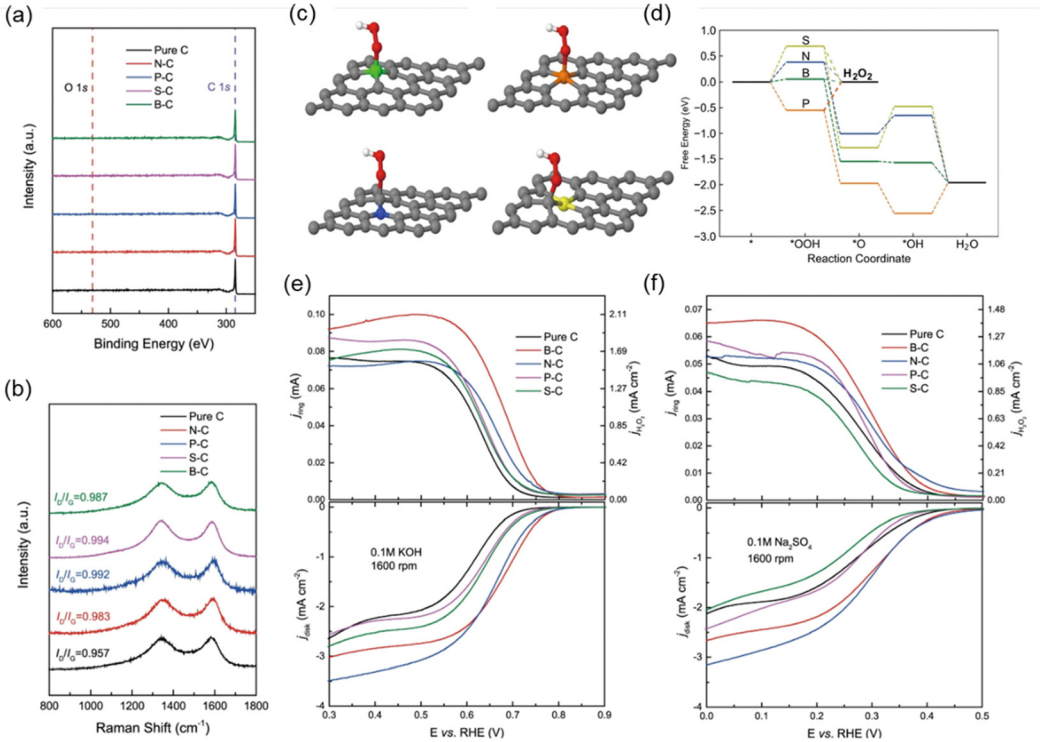

Fig. 8 Heteroatom-doped carbon catalysts for electrocatalytic H_2O_2 generation. (a) XPS survey scan and (b) Raman spectroscopy for pure C and B, N, P, S-doped carbon catalysts; (c) preferred *OOH adsorption configurations on B-, P-, N-, and S-doped graphene, respectively. Green, orange, blue, yellow, gray, red, and white spheres represent B, P, N, S, C, O and H, respectively; (d) free-energy profile of O_2 reduction paths (U_{RHE} = 0.7 V); LSV curves and H_2O_2 currents (1.2 V *vs.* RHE) recorded by RRDE in (e) 0.1 M KOH and (f) 0.1 M Na_2SO_4. Reproduced with permission from ref. 81. Copyright 2021, Nature Publishing Group.

hierarchical porous boron-doped carbon (B-DC) electrocatalyst was synthesized from fullerene (C_{60}) frameworks and boric oxide.[107] Befitting from boron doping and abundant topological pentagon defects, the B-DC catalysts exhibited a high ORR onset potential of 0.78 V and a $2e^-$ selectivity over 95%. Remarkably, the B-DC electrocatalyst-based device achieved a remarkable H_2O_2 yield rate of 247 mg L^{-1} h^{-1} and a quantitative Faraday efficiency of nearly 100%. For sulfur-doped defective nanocarbons (S-DNC), a similar high ORR onset potential (0.78 V) and selectivity (90%) was obtained, with an superior H_2O_2 yield rate of 690 mg L^{-1} h^{-1} in a H cell.[113] In 2023, Lu *et al.*[102] designed and fabricated a pentagonal defect-rich N-doped carbon nanomaterial (PD/N–C) *via* pyrolysis of C_{60} as the precursor followed by ammonia treatment (Fig. 9a). A great number of mesopores and micropores were created in PD/N–C, along with abundant irregular folds and curved edges (Fig. 9b–d). Moreover, the aberration-corrected scanning TEM (AC-STEM) and the corresponding fitting results (Fig. 9e–j) further demonstrate that the PD/N–C sample contains rich pentagon defects. As a result, the PD/N–C catalysts achieved excellent $2e^-$ ORR activity, selectivity, and stability in acidic electrolytes, even outperforming the Pt–Hg alloy catalyst. The linear sweep voltammetry curves (Fig. 9k) show that the PD/N–C catalyst achieves a larger ORR current density (3.1 mA cm^{-2} at 0 V) along with a higher onset potential in a wide potential range from 0 to 0.6 V, as compared to the N-doped carbon nanomaterial dominated by hexagon graphene nanosheets (N–GNS). This performance is among the top of all reported metal-free carbon-based catalysts and even superior to some noble-metal-based catalysts and the benchmark $PtHg_4$ alloy catalyst in acidic electrolytes (Fig. 9l). By comparing a series of samples, the synergetic effects of both topological defects and N-doping are responsible for the superb $2e^-$ ORR performance of the PD/N–C catalysts (Fig. 9m and n).

In addition to single-element doping, dual element co-doping on carbon materials has received increased research attention toward the electrocatalytic $2e^-$ ORR due to the unique synergistic effect.[114] For instance, a yolk–shell B/N co-doped hollow carbon nanosphere, with oxygen-vacancy decorated reduced graphene oxide coating (B/N-HCNS@VO-G) was reported as an efficient metal-free electrocatalyst for the $2e^-$ ORR with high durability.[115] Such a dual-doping electrocatalyst leads to excellent electrocatalytic H_2O_2 production performance with a high selectivity of 91% and yield of 56 ppm (0.7 V), allowing *in situ* antibiotic and dye degradation for on-site wastewater remediation. Very recently, pentagon-S and pyrrolic-N coordinated (SNC) graphene with in-plane topological defects was synthesized through a two-step hydrothermal and nitridation procedure (Fig. 10).[99] The SNC is composed of stained hexagons with sporadic pentagons (Fig. 10d–g), suggesting that the hexagonal topological structure of the carbon matrix is significantly distorted. In addition, the dual-doping of S and N elements introduces unsymmetrical dumbbell-like S–C–N motifs, which can effectively tune the electronic structures of graphene (Fig. 10h and i).

Open Access Article. Published on 21 April 2025. Downloaded on 6/16/2026 6:54:28 AM.
This article is licensed under a Creative Commons Attribution-NonCommercial 3.0 Unported Licence.

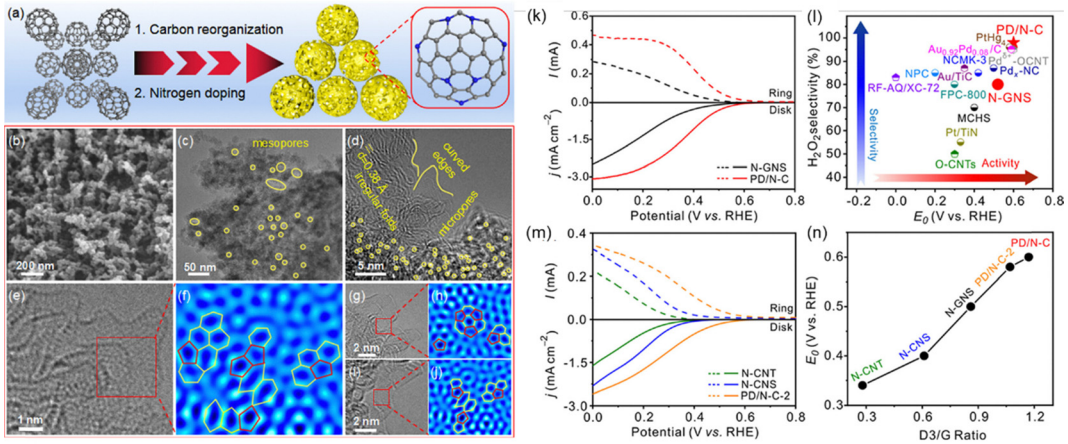

Fig. 9 Pentagonal defect-rich N-doped carbon nanomaterial (PD/N–C) using fullerene (C_{60}). (a) Schematic of the synthesis of PD/N–C; (b) SEM, (c) and (d) TEM, and (e), (g) and (i) AC-STEM images and (f), (h) and (j) the corresponding Fourier transform fitting results of PD/N–C; (k) RRDE polarization curves and H_2O_2 currents at the ring electrode of PD/N–C and N–GNS; (l) comparison of the $2e^-$ ORR performance of representative electrocatalysts; (m) RRDE polarization curves and H_2O_2 currents at the ring electrode of N–CNT, N–CNS, and PD/N–C-2; (n) onset potential (E_0) as a function of the D3/G ratio of a series of samples. Reproduced with permission from ref. 102. Copyright 2023, the American Chemical Society.

Theoretical calculations further unveiled that the defective S–C–N motifs can effectively optimize the binding strength to the OOH* intermediate and reduce the energy barrier for the ORR to H_2O_2 (Fig. 10j). As a result, the SNC catalyst exhibited ultrahigh H_2O_2 production rates of 8100, 7300, and 3900 mmol g^{-1} h^{-1} in alkaline, neutral, and acidic electrolytes, respectively.

It is worth mentioning that heteroatom doping into the carbon matrix could also induce surface functional groups. For example, oxygen functionalization onto the parent carbon structures has been reported to be effective to improve $2e^-$ ORR performance.[21,116,117] For instance, oxygen-doped carbon dots (O-CDs) were synthesized using a solvent engineering approach and exhibited excellent catalytic activity.[118] By tuning the ratio of ethanol and acetone solvents during the synthesis, the surface electronic structure of the resulting O-CDs can be precisely modulated. The selectivity and activity of the O-CDs were strongly dependent on the amount of edge active C–O groups, achieving the highest H_2O_2 selectivity of up to ~96.6% (n = 2.06, 0.65 V *vs.* RHE) and an ultralow Tafel slope of 64.8 mV dec^{-1}.

Despite tremendous works on doped carbon materials for electrocatalysis H_2O_2 production, the dynamic structural transformation of these materials during the electrocatalysis reaction process has received less attention. Active site identification in carbon materials is crucial for understanding the mechanism, but resolving precise configuration of active sites remains a huge challenge. In 2023, Wu *et al.*[119] manipulated the defect

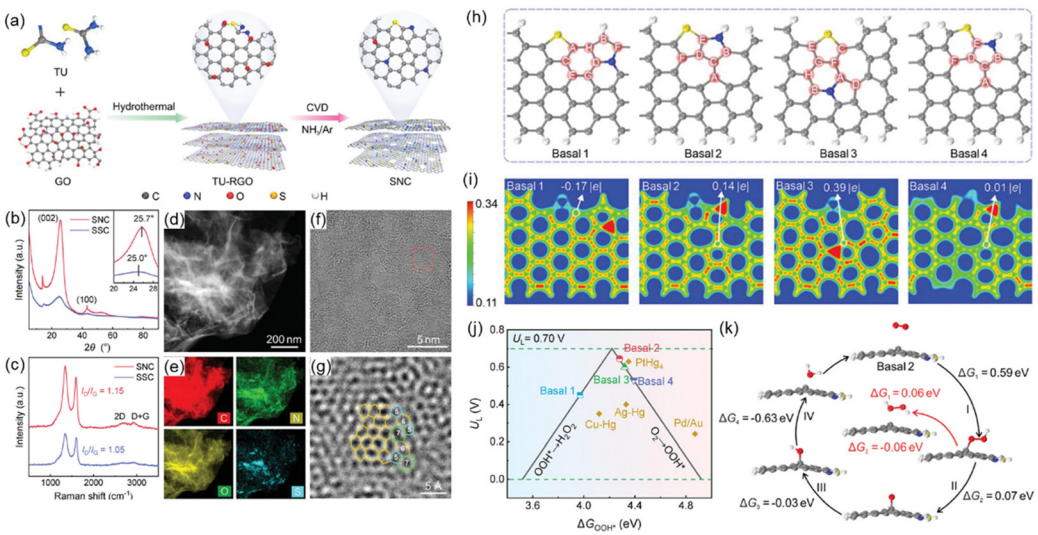

Fig. 10 Pentagon-S and pyrrolic-N coordinated (SNC) graphene with in-plane topological defects. (a) Schematic illustration of synthesis for graphene pentagon-S and pyrrolic-N coordinated (SNC); (b)–(g) XRD patterns, Raman spectra, TEM images, and EDS mappings; (h) computational models, (i) Bader charge, (j) activity-volcano plot (U_L = 0.70 V), and (k) ORR reaction pathway diagrams and corresponding energy barriers for each step on Basal 2. Reproduced with permission from ref. 99. Copyright 2024, Wiley-VCH.

 This journal is © The Royal Society of Chemistry 2025

Open Access Article. Published on 21 April 2025. Downloaded on 6/16/2026 6:54:28 AM.
This article is licensed under a Creative Commons Attribution-NonCommercial 3.0 Unported Licence.

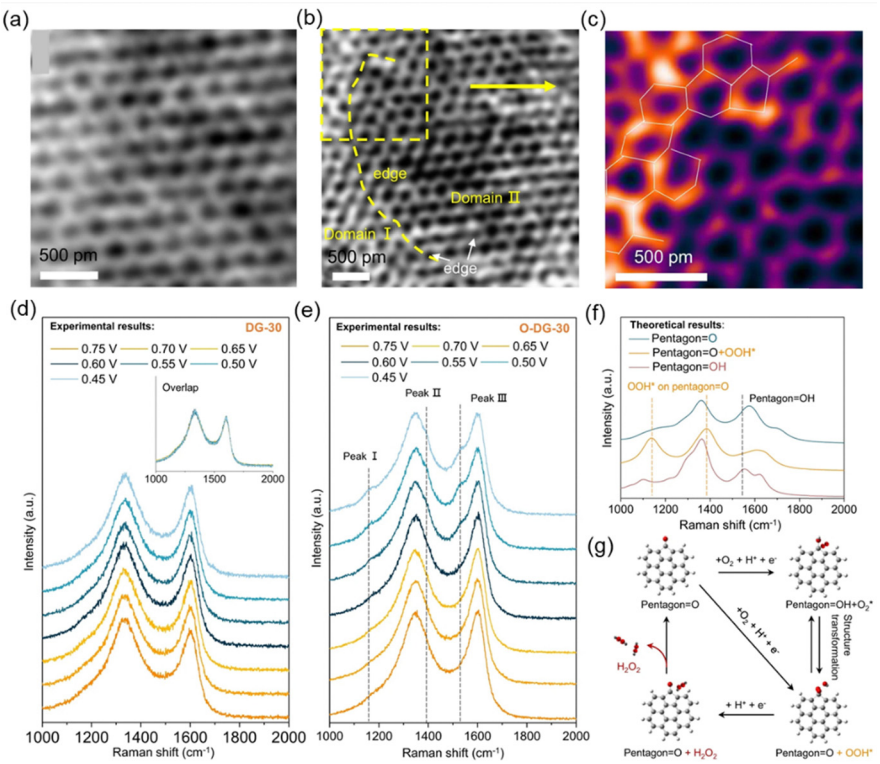

Fig. 11 *In situ* investigation of dynamic active sites in oxygen modified defective graphene (O-DG) electrocatalysts. iDPC-STEM image of O-DG-30 in (a) perfect domain and (b) and (c) defective domain; *in situ* Raman spectra of (d) DG-30 and (e) O-DG-30 on a flow cell in O_2-saturated 0.1 M KOH; (f) the calculated Raman spectra of three possible atomic structures of the O-groups and relevant surface species on defective graphene; (g) schematic diagram of the possible electrocatalytic mechanism of O-DG. Reproduced with permission from ref. 119. Copyright 2023, Nature Publishing Group.

density and oxygen groups on graphene, and revealed the oxygen group redistribution and positive correlation relationship between the defect density and their ORR performance (Fig. 11). The dynamic evolution processes of defects were monitored through *in situ* Raman, FTIR and XPS technologies, combined with theoretical simulations. The results clarified the configuration of major active sites (carbonyl on pentagon defect) and key intermediates (*OOH), providing deep understanding of the catalytic mechanism for doped defective carbon materials.

3.3. Hybrid systems

3.3.1. Carbon–semiconductor heterostructures. Recently, several studies have been reported on the coupling of carbon-based materials with metal oxides or nitrides to boost their $2e^-$ ORR activity.[120–126] Generally, the structural modulation of the carbon–metal oxide nanocomposites can rapidly release *OOH generated by the metal oxides with high activity. For instance, Qu *et al.*[120] reported the integration of CNTs with g-C_3N_4 to improve both electrocatalytic activity and selectivity of CNTs for H_2O_2 production by forming a π–π interaction at their interface. The optimal g-C_3N_4/CNT nanocomposite catalyst exhibited almost unity (~97%) for H_2O_2 production at 0.50 V *vs.* RHE with a 2 times current density of the pristine g-C_3N_4 or CNT. The enhanced activity can be attributed to the synergistic effect, with which g-C_3N_4 provides active sites to activate O_2 while CNT offers channels to facilitate electron transfer. In addition, Guo *et al.*[127] designed and prepared a novel MnO_x@Carbon hybrid electrocatalyst by calcinating polymer-manganese-metal–organic framework (polyMn-MOF) as the precursor under an N_2 atmosphere. DFT calculation revealed that the optimized MnO_x@Carbon sample exhibited optimized adsorption energy of *OOH, with a high H_2O_2 selectivity of 96.5% and a large ORR current of 2.3 mA cm^{-2}.

Recently, Xue *et al.*[121] reported a novel p–n heterojunction nanocomposite consisting of N-doped carbon and Co_3O_4 (NC@Co_3O_4), for efficient electrocatalytic H_2O_2 production (Fig. 12). Increasing the Co content results in a more positive flat band potential (E_{fb}), indicating a decrease of the Fermi level. In addition, the differential charge density calculation demonstrated that the electrons of the NC are transferred to the Co_3O_4 and promotes the affinity of the O atom of H_2O_2 at the electron deficient carbon sites in NC, which facilitates the cleavage of O–O bonds. Consequently, the •OH generation rate catalyzed by NC@Co_3O_4 was 6.5 times of that by bare NC. This work highlights the promising potential of constructing carbon/semiconductor nanocomposites toward efficient H_2O_2 generation.

3.3.2. Atomic-site engineered carbon hybrids. Atomically dispersed transition metals single-atom catalysts (SACs) coordinated within a carbon matrix have proven to be effective ORR electrocatalysts, featuring a nearly 100% utilization of metal atoms as active sites and excellent catalytic activity.[128,129] The electronic structure of the SACs can be regulated benefiting from the strong interaction between metal atoms and the substrate, and further modulates the adsorption energy of the catalyst for oxygen-containing intermediates, which affects the

Open Access Article. Published on 21 April 2025. Downloaded on 6/16/2026 6:54:28 AM.
This article is licensed under a Creative Commons Attribution-NonCommercial 3.0 Unported Licence.

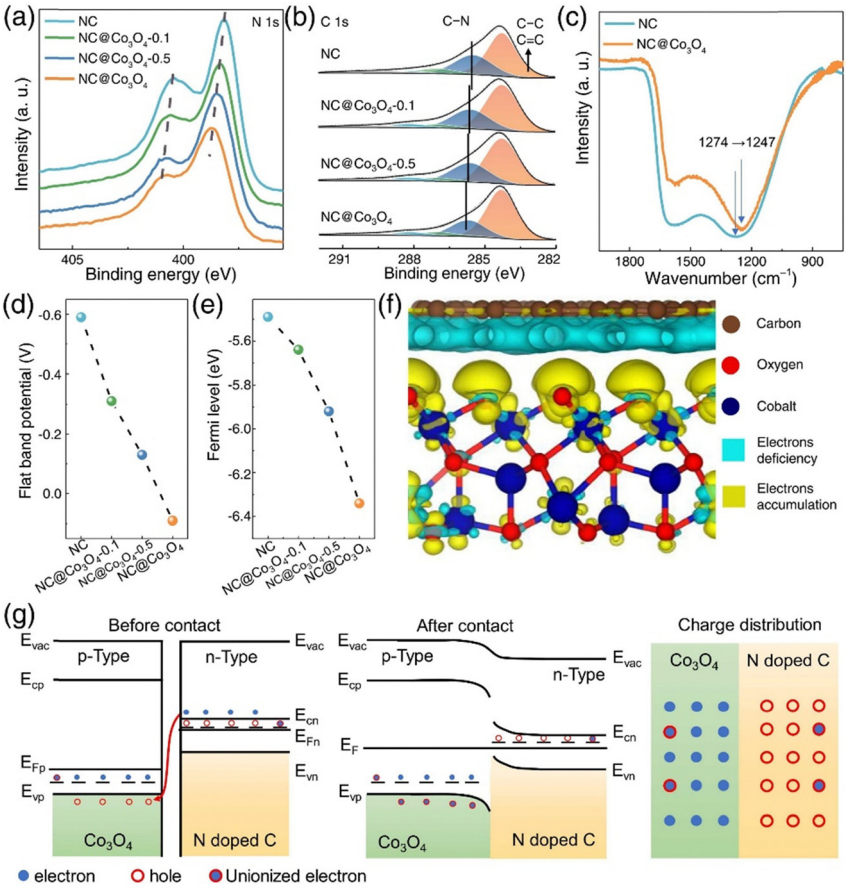

Fig. 12 N-doped carbon and Co_3O_4 (NC@Co_3O_4) p–n heterojunction nanocomposite for electrocatalytic H_2O_2 production. XPS spectra of (a) N 1s and (b) C 1s; (c) FTIR spectra of NC and NC@Co_3O_4; (d) the flat band potential (E_{fb}) estimated from Mott–Schottky plots; (e) Fermi level measured by UPS; (f) differential charge density of the NC@Co_3O_4 heterojunction; (g) schematic illustration of the energy band and electron transfer of the NC@Co_3O_4 p–n heterojunction. Reproduced with permission from ref. 121. Copyright 2024, Elsevier.

$2e^-$ ORR selectivity.[130–134] As such, different SACs such as Co-SACs,[133,135–138] Zn-SACs,[131] Fe-SACs,[139] Mn-SACs,[140] W-SACs,[141] Pt-SACs,[142,143] Pd-SACs,[82,91] Pb-SACs,[144] Sn-SACs[145] and In-SACs[146] have displayed superior $2e^-$ ORR performances for H_2O_2 production, showing large mass activity, low overpotential, and high selectivity. In this part, we emphasize the most important achievements in this field by presenting and discussing both experimental and theoretical investigations, especially the most recent advancements on more complex systems using dual-single atom carbon catalysts or coupled with other synergistic effects.

Gao *et al.*[147] fabricated transition metal (Mn, Fe, Co, Ni, and Cu) SAC anchored N-doped graphene and systematically investigated their electrocatalytic performance for synthesizing H_2O_2 *via* the ORR (Fig. 13a). Theoretical simulations demonstrated that the Co-SAC possesses optimal d-band center, activity-volcano plot, and adsorption energy of the *OOH intermediate among all M-SAC samples (Fig. 13b–d). As a result, the kinetic current for H_2O_2 production using the Co SAC catalyst can reach up to $\sim$1 mA cm^{-2} (0.6 V *vs.* RHE in 0.1 M $HClO_4$) with Faraday efficiency over 90% (Fig. 13e and f), which even outperforms state-of-the-art noble-metal-based electrocatalysts in acidic media. Moreover, kinetic and *in situ* X-ray absorption analysis demonstrated that the N-coordinated single Co single-atom function as the active site for the reaction, which is rate-limited by the first electron transfer step.

Compared to well-studied SACs, dual-atom catalysts (DACs) have received considerable attention due to the synergistic interactions between two adjacent metal sites, leading to remarkably enhanced activity, selectivity, and stability. The dual sites facilitate multi-step reactions and improve binding energies for reactants and products. In addition, DACs are more resistant to aggregation and can offer tunable properties through metal pair selection, making them ideal for complex catalytic processes. Recent advancements in DAC design have demonstrated their superior electrocatalytic performance for H_2O_2 production through the $2e^-$ ORR pathway.

In-N-C DACs were proposed by Du *et al.*[148] as effective $2e^-$ ORR catalysts for producing H_2O_2 in acidic media. The DFT calculations indicate that the valence electron number and the d-band center of the Co 3d orbital can be modulated by OH-blocked In, which leads to moderate adsorption of the OOH intermediate on neighboring Co and favors $2e^-$ ORR kinetics of Co/In-N-C DACs. As a result, a partial current density of

 This journal is © The Royal Society of Chemistry 2025

Open Access Article. Published on 21 April 2025. Downloaded on 6/16/2026 6:54:28 AM.
This article is licensed under a Creative Commons Attribution-NonCommercial 3.0 Unported Licence.

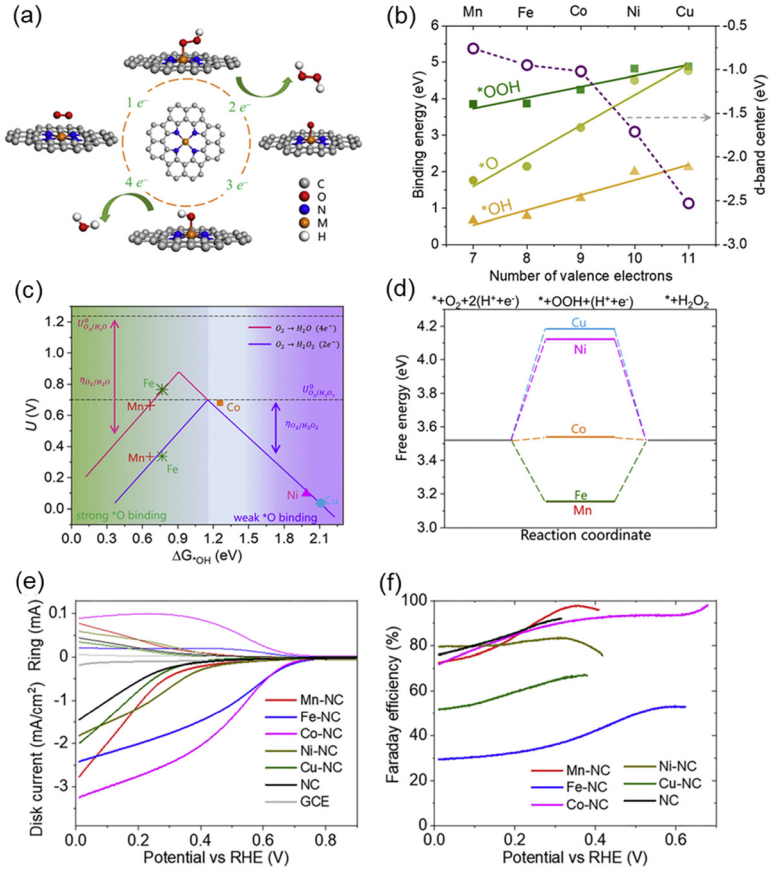

Fig. 13 Transition metal SACs (M-SAC) (M = Mn, Fe, Co, Ni, and Cu) anchored in N-doped graphene electrocatalysts for producing H_2O_2. (a) Schematic of the ORR; (b) binding energy of *OOH, *O, and *OH on M-SAC and d-bond center of different M atoms in M-SAC; (c) volcano curves of the ORR *via* the $2e^-$ and $4e^-$ pathways; (d) free energy diagrams of the $2e^-$ ORR on different M-SACs (0.7 V *versus* RHE); (e) LSV curves and (f) faradaic efficiency as a function of potential. Reproduced with permission from ref. 147. Copyright 2020, Cell Press.

1.92 mA cm^{-2} (0.65 V in the RRDE test) was obtained, with a H_2O_2 production rate as high as 9680 mmol g^{-1} h^{-1} in a three-phase flow cell. Very recently, Yang *et al.*[84] fabricated heteronuclear CoZn DACs confined in N,O-doped hollow carbon nanotube reactors ($CoZn_{SA}$@CNTs) (Fig. 14). The differential partial charge density calculation demonstrated that the dual-atom centers in $CoZn_{SA}$@CNTs possess more charges than Co_{SA}@CNTs (Fig. 14a), indicating a rearrangement of the local charge distribution to facilitate the adsorption of OOH* after introducing Zn. The decrease of the d-band center in CoZn-SA@CNTs resulted in the appropriate adsorption of OOH* for H_2O_2 generation (Fig. 14b), while inhibiting the breakage of O–O bond to produce H_2O, ultimately facilitating the $2e^-$ ORR. In addition, the $CoZn_{SA}$@CNT model exhibited a more favorable ΔG_{OOH^*} than Co_{SA}@CNTs (Fig. 14c and d). The well-designed $CoZn_{SA}$@CNT nanocomposite displayed outstanding electrocatalytic reactivity/selectivity for generating H_2O_2 in the whole pH range (Fig. 14e–g), with a higher $2e^-$ ORR selectivity for H_2O_2 production than Co_{SA}@CNTs and Zn_{SA}@CNTs. In a H-type cell, $CoZn_{SA}$@CNTs/carbon fiber felt reached nearly 100% H_2O_2 selectivity in the range of 0.2–0.65 V (*vs.* RHE) with a yield rate of 1500 mmol g^{-1} h^{-1}, surpassing most of the reported SACs. These studies highlight the great advantages of using DACs/carbon for highly efficient and selective H_2O_2 production.

3.4. Synergistic integration of multiple effects

The integration of different effects, such as morphological control, defect engineering, and single-atom site design, creates a synergistic interplay that elevates the catalytic performance beyond the simple sum of individual components. The coupling effect simultaneously enhances mass transport efficiency, electronic structure modulation, and atomic-level active site utilization, collectively optimizing the reaction pathways and maximizing overall catalytic efficiency. Below, we discuss key coupling strategies to date, providing insights to guide future advancements in rational design of carbon-based electrocatalysts.

3.4.1. Coupling defect/surface groups with microstructures. Carbon materials with diverse porous structures have been reported, with simultaneous introduction of surface functional groups. For instance, Albashir *et al.*[149] fabricated mesoporous material (Meso-PC) functionalized with a ketonic carbonyl (–C═O) group, which exhibits outstanding $2e^-$ ORR selectivity (~100%) at a potential of 0.4 V_{RHE}. This can be attributed to its

Open Access Article. Published on 21 April 2025. Downloaded on 6/16/2026 6:54:28 AM.
This article is licensed under a Creative Commons Attribution-NonCommercial 3.0 Unported Licence.

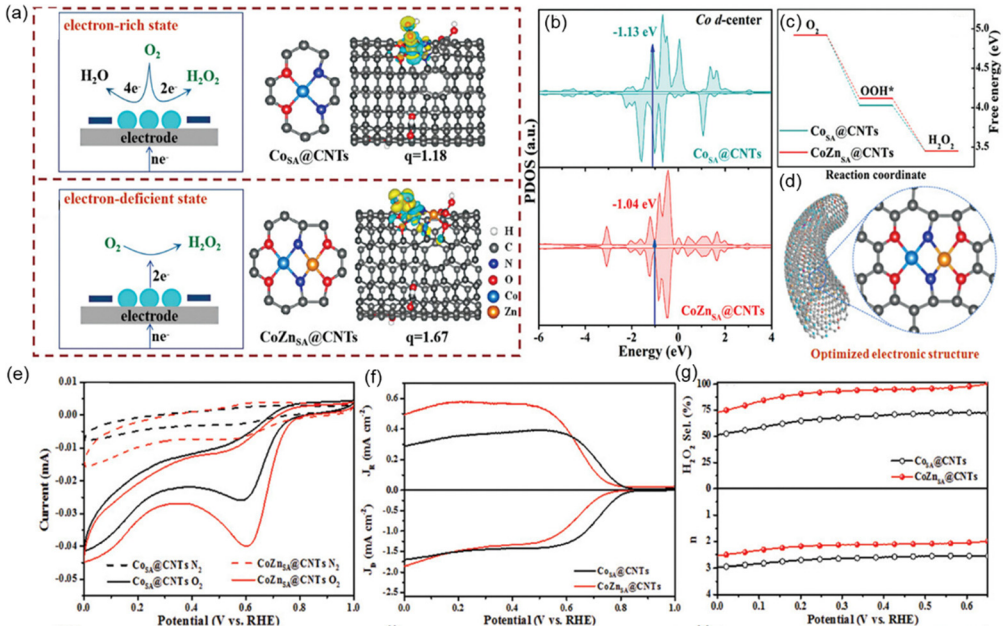

Fig. 14 CoZn DACs confined in N,O-doped hollow carbon nanotube reactors ($CoZn_{SA}$@CNTs) for electrocatalytic synthesis of H_2O_2. (a) Illustration of the model and their differential partial charge densities with OOH* adsorption (side view); (b) PDOS of the Co 3d orbital and (c) Gibbs free energy diagrams of the two-electron ORR of Co_{SA}@CNTs and $CoZn_{SA}$@CNTs, respectively; (d) schematic of the optimized electronic structure; electrochemical performance of $CoZn_{SA}$@CNTs and Co_{SA}@CNTs: (e) CV curves, (f) LSV curves based on RRDE, and (g) H_2O_2 selectivity and electron transfer number (*n*). Reproduced with permission from ref. 84. Copyright 2024, Wiley-VCH.

precisely tailored pore structure, which facilitates the mass transfer of reactants and products. Furthermore, studies suggest that the –C═O group serves as the primary active site for the $2e^-$ ORR, while a moderate surface concentration of oxygen functionalities is crucial to enhancing electrochemical H_2O_2 synthesis activity.

In addition, Jing *et al.*[89] demonstrated that N,O co-doped carbon nanosheets (N,O-CNS) with a hierarchical micro/mesoporous structure can create an oxygen-rich, locally alkaline-like microenvironment, significantly promoting the $2e^-$ ORR pathway in a neutral medium. Their study revealed that the hierarchical architecture not only elevates the local pH near the active sites but also facilitates the formation of intermediates ($*O_2$ and *OOH), thereby enhancing H_2O_2 selectivity and yield. Remarkably, the optimized N,O-$CNS_{0.5}$ catalyst achieved an exceptional H_2O_2 production rate of 6705 mmol g^{-1} h^{-1} in a flow cell, setting a new benchmark for neutral-media electrocatalysis. This work highlights the critical role of synergistic microenvironment engineering, which combines pore structure control, heteroatom doping, and local pH modulation, in designing high-performance electrocatalysts for sustainable H_2O_2 synthesis.

3.4.2. Coupling atomic active sites with microstructures. Coupling SACs with other tailoring strategies such as microstructure modulation of carbon materials can lead to novel synergistic effects to further boost the electrocatalytic performance. A notable example involves atomically dispersed Co/Mo sites anchored on mesoporous carbon hollow spheres (Co/Mo-MCHS) synthesized *via* a template-engaged strategy, which exhibit high selectivity for the ORR toward H_2O_2 production in acidic media.[150] Benefitting from the electron-donating effect of Mo atoms, an enriched electron density around the Co center for Co/Mo-MCHS is observed, resulting in optimal adsorption of the key *OOH intermediates to approach the apex of $2e^-$ ORR volcano plot. Moreover, the introduction of Mo species simultaneously suppresses the electroreduction of as-obtained H_2O_2 on Co sites. Owing to the integration of mesoporous hollow merits and the electron-donating effect, the Co/Mo-MCHS electrocatalyst exhibits an efficient $2e^-$ ORR pathway with a noticeable ring current response and a high H_2O_2 selectivity of 90–95% over the wide potential range in acidic media. After long-term operation over 15 h, 90% of the initial H_2O_2 selectivity could be retained. For large-scale electrolysis, a remarkable H_2O_2 yield of 2102 mg for 150 h is obtained, suggesting great potential for practical applications. This study provides valuable guidance for the rational design of more complex SACs/carbon catalysts by combing different effects in the future.

3.4.3. Coupling electronic defects with atomic active sites. Liu *et al.*[151] systematically investigated a series of metal catalysts anchored on nitrogen-doped carbon (M–NC), including representative transition metals (Mn, Fe, Co, and Ni), 4d transition metal (Ru), 5d transition metal (Pt), and non-transition metal (In), to assess their activity for synthesizing H_2O_2 (Fig. 15). Four types of M–NC catalysts with different pyridine and pyrrole N atoms ratios were constructed (Fig. 15a). The $2e^-$ ORR activity volcano plots for 40 SAC configurations were examined through DFT calculations (Fig. 15b). The coordination environment can tune the ΔG_{*OOH} position in M–NCs significantly, with the highest value occurring for $MN_{(Po)4}$ type catalysts for each metal. Meanwhile, the corresponding ΔG_{*OH} and $2e^-$ WOR volcano curve were also calculated (Fig. 15c), demonstrating that pyrrolic-N affects the

 This journal is © The Royal Society of Chemistry 2025

Open Access Article. Published on 21 April 2025. Downloaded on 6/16/2026 6:54:28 AM. This article is licensed under a Creative Commons Attribution-NonCommercial 3.0 Unported Licence.

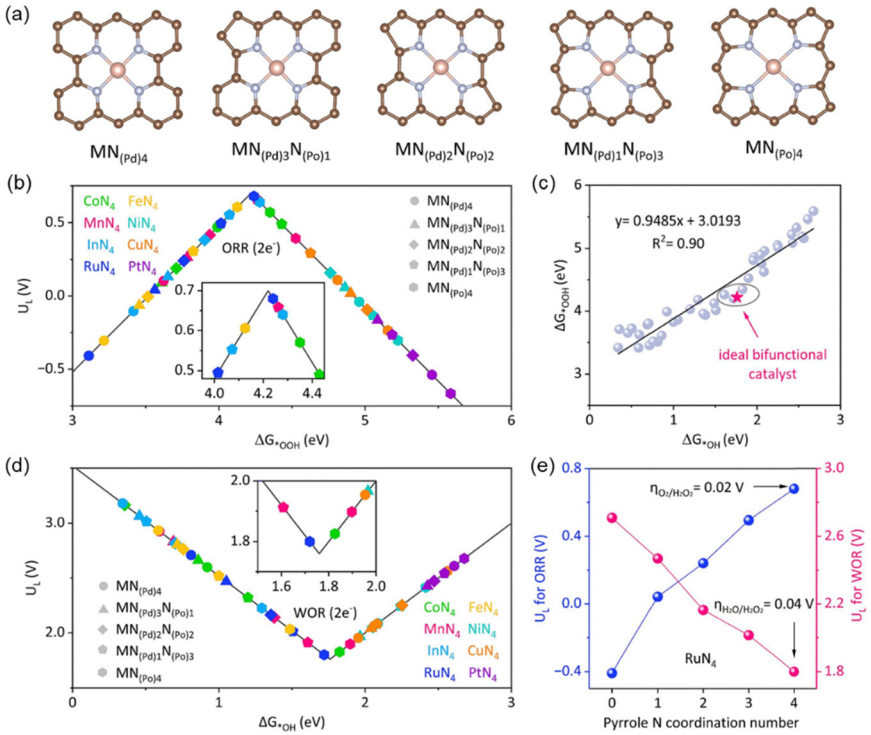

Fig. 15 DFT calculation on various metal SAC catalysts anchored on nitrogen-doped carbon (M–NC) for H_2O_2 production *via* 2e$^-$ ORR and 2e$^-$ WOR. (a) Optimized MN_4 structure with different pyrrole N coordination numbers; activity volcano relation for (b) 2e$^-$ ORR and (c) 2e$^-$ WOR between intermediates' formation energy and limiting potential; (d) scaling plots between ΔG_{*OH} and ΔG_{*OOH}; (e) relationship between pyrrole N coordination numbers and limiting potential for 2e$^-$ ORR and 2e$^-$ WOR of all Ru-NC catalysts. Reproduced with permission from ref. 151. Copyright 2023, Elsevier.

adsorption of OH, and the free energy shift is almost consistent with *OOH. Considering the ORR and WOR reaction pathway together, the $CoN_{(Po)4}$, $MnN_{(Pd)1}N_{(Po)3}$ and $RuN_{(Po)4}$ show promising prospects as bifunctional SAC for H_2O_2 generation. Considering the fitting curve of ΔG_{*OH} and ΔG_{*OOH} (Fig. 15d) and all key factors including overpotential, reaction kinetics, transition state energy, and thermodynamic stability, $RuN_{(Po)4}$ SACs are the most promising candidates for efficient H_2O_2 generation, and the pyrrole N coordination can modulate the 2e$^-$ ORR/WOR kinetics (Fig. 15e). This study provides deep theoretical insights into regulating the coordination structure for the rational design of highly efficient and stable bifunctional SACs/carbon catalysts for H_2O_2 production.

3.4.4. Multiple synergistic effects. The integration of multiple effects creates a powerful synergistic platform that overcomes the limitations of binary coupling, which can further maximize the overall catalytic efficiency. A representative example involves the rational design of highly porous open carbon nanocages with embedded Co nanoparticles (NPs) fabricated through a template-assisted method.[152] The optimized P-Co@C-700 catalyst exhibits several integration effects, including highest percentage of –C–O–C group and defects, embedding Co NPs, and mesoporous structures, resulting in a high selectivity of up to 94% toward H_2O_2 production in 0.1 m $HClO_4$. Benefiting from the synergistically modulated electronic and pore structures, the optimized open carbon nanocages exhibit outstanding activity, selectivity, and stability for 2e$^-$ H_2O_2 production under acidic conditions.

Moreover, as a notable example, Dong *et al.*[140] developed a novel Mn SAC-coordinated boundary-rich porous carbon-based electrocatalyst (Fig. 16a and b), in which the secondary coordinated epoxide, hydroxyl groups surrounding the $Mn–N_3–O$ centers, and the boundary-rich morphology together lead to the predominant selectivity and efficiency for H_2O_2 production through the 2e$^-$ ORR pathway. The catalysts exhibited nearly 100% faradaic efficiency and with a reaction rate up to 15 100 mmol g_{cat}^{-1} h^{-1} (0.1 V *vs.* RHE), achieving the record activity for the Mn-based electrocatalyst in the electrosynthesis of H_2O_2 (Fig. 16c–e). Mechanistic investigations indicate that the epoxide and hydroxyl groups surrounding the Mn(II) centers promote the spin state and tailor the adsorption of the *OOH intermediate, and multiscale simulations reveal that the high-curvature boundaries can promote adsorption and local enrichment of O_2 (Fig. 16f–j). Such synergy highlights the importance of holistic material design, where defects, doping, and atomic-scale engineering work in concert to achieve greatly improved performance.

To comprehensively evaluate the advantages and limitations of carbon-based electrocatalysts for H_2O_2 production, it is essential to compare them with non-carbon-based catalyst systems, such as metal oxides and noble-metal catalysts. Table 1 summarizes the critical metrics (onset potential, H_2O_2 selectivity, production rate, and stability) across different representative catalyst types. Although Pt/Pd-based noble metal-based catalysts are recognized as efficient catalysts with small overpotential and high selectivity

Open Access Article. Published on 21 April 2025. Downloaded on 6/16/2026 6:54:28 AM.
This article is licensed under a Creative Commons Attribution-NonCommercial 3.0 Unported Licence.

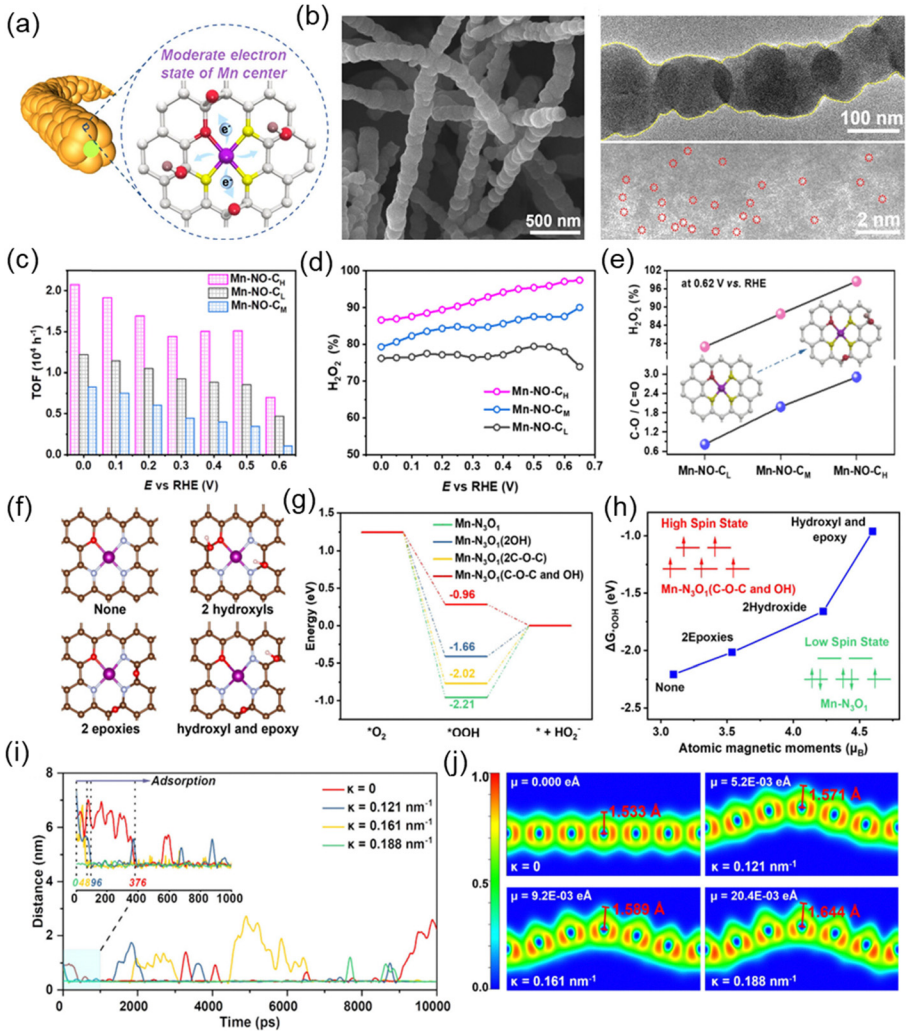

Fig. 16 (a) The schematic of the heterogeneous catalyst composed of boundary-rich carbons supported active Mn(II) centers (Mn–NO–C_H) with selective oxygen functional groups. (b) SEM, TEM and HAADF-STEM images of Mn–NO–C_H. (c) TOFs, (d) H_2O_2 selectivity, and (e) correlation between H_2O_2 selectivity (0.62 V *vs.* RHE) and the proportion of oxygen species. (f) The DFT models for Mn–N_3O_1. (g) The calculated free energy at 0 V *vs.* RHE for the 2e-ORR pathway. (h) The correlation between the magnetic moment and the free energy for Mn–N_3O_1 after *OOH adsorption. (i) MD simulation for the minimum distance between O_2 molecules and C atoms. (j) Electronic localization function mapping images with different curvatures. Reproduced with permission from ref. 140. Copyright 2024, Wiley-VCH.

Table 1 Comparison of performance with representative non-carbon-based systems

Type	Catalysts	Selectivity (%)	H_2O_2 production rate	Electrolyte	Stability	Ref.
Noble metals	PtP_2	98.5	2.26 mmol h^{-1} cm^{-2}	0.1 M $HClO_4$	120 h	157
	Pt–Hg/C	>90	—	0.1 M $HClO_4$	8000 cycles	24
	Pt_1–CuS_x	92–96	546 mmol g^{-1} h^{-1}	0.1 M $HClO_4$	10 h	158
	$Pt_1/CoSe_2$	—	110.02 mmol g^{-1} h^{-1}	0.1 M $HClO_4$	60 h	159
Oxides	h-SnO_2	99.9	3885.26 mmol g^{-1} h^{-1}	0.1 M Na_2SO_4	20 h	156
	α-Fe_2O_3	80.5	546.8 mmol g^{-1} h^{-1}	0.1 M KOH	48 h	155
Carbon-based	Single atoms-carbon	96.5	12 510 mmol g^{-1} h^{-1}	0.1 M KOH	12 h	139
	N/S-CNTs	90.0	30 370 mmol g^{-1} h^{-1}	1.0 M KOH	200 h	160
	B-doped carbon	88.7	24 300 mmol g^{-1} h^{-1}	0.1 M KOH	100 h	161
Other systems	MOF nanosheets	99	6500 mmol	0.1 M KOH	11 h	162
	Boron nanosheets	~90	25 100 mmol g^{-1} h^{-1}	1.0 M Na_2SO_4	140 h	163

for the $2e^-$ ORR, their industrial-scale application is greatly limited by scarcity, high cost, and susceptibility to poisoning.[24,41,153,154] Metal oxide electrocatalysts demonstrate excellent stability, while achieving high selectivity remain challenging.[155] Although some recently reported metal oxides such as h-SnO_2 demonstrate excellent electrocatalytic activity,[156] they still suffer from poor stability

Open Access Article. Published on 21 April 2025. Downloaded on 6/16/2026 6:54:28 AM. This article is licensed under a Creative Commons Attribution-NonCommercial 3.0 Unported Licence.

in electrolyte. Furthermore, synthesizing highly active metal oxide catalysts often requires complex procedures and precise control over their structure and composition. It is also worth noting that the emerging MOF/COF materials show high production activity but poor stability.

We have summarized the most representative carbon-based materials for electrocatalytic H_2O_2 production reported in the past few years (Table 2), systematically classified by materials design categories: microstructure tailoring, defect engineering (including intrinsic and heteroatom doping), surface functional group modulation, single-atomic site configurations, and synergistic effects. In comparison, carbon-based electrocatalysts offer distinct advantages, including low-cost and wide availability, making them highly attractive for large-scale applications. Up till now, the performance of carbon-based electrocatalyst is comparable or even outperforming those of many noble metal-based systems, maintaining cost and environmental benefits. Carbon-supported single-atom catalysts (SACs) achieve high production rates of $\sim$500–30 000 mmol g^{-1} h^{-1}. However, the activity and stability of carbon catalysts in neutral or weakly acidic environments still need to be further improved, as well as mitigating degradation during long-term electrochemical operation.

The stability of carbon-based electrocatalysts for H_2O_2 production varies significantly across different categories, with durations ranging from a few hours to $\sim$250 h. Microstructure-modulated catalysts like graphitic ordered mesoporous carbon (O-GOMC) exhibit high stability (168 h) due to robust porous frameworks, while defect-engineered materials such as B-doped carbon demonstrate durability (100 h) under high current densities. Surface modifications, including polymer coatings or metal complexes, demonstrated relatively low stability as evidenced by CoPc-carbon (24 h). Although single-atom catalysts generally exhibit very short lifetime ($\sim$10 h), recently reported synergistic systems such as Pb SAs/OSC (100 h) and N,S-rich carbon nanotubes (200 h) are highly promising. Challenges still remain in standardizing testing protocols and achieving long-term stability for industrial applications. Future research should focus on elucidating degradation mechanisms and optimizing catalyst designs for extended operational lifetimes.

4. Conclusions and perspective

The electrochemical production of H_2O_2 using carbon-based nanomaterials has gained considerable research attention as an environmentally friendly, low-cost and efficient method. Substantial efforts have been made both experimentally and theoretically on $2e^-$ ORR electrocatalysis, with a focus on the structure–property relationship and design of efficient carbon-based electrocatalysts. In this review, we summarized the key advancements in the materials design strategy. These studies demonstrate that modifying the local atomic structure of carbon materials, incorporating functional surface groups, doping with foreign atoms, tailoring the microstructure, and introducing semiconductor or single-atomic sites can enhance not only the activity and selectivity for H_2O_2 production but also the long-term stability of these catalysts. These developments open the door to more efficient and scalable electrocatalytic processes for green H_2O_2 production.

Despite the considerable progress achieved, challenges remain for the industrial-scale implementation of electrocatalytic H_2O_2 production using carbon-based materials, including improving electrocatalytic activity, ensuring long-term stability, and developing practical designs for carbon-based electrodes and reactors. Therefore, advancing carbon electrocatalyst design to achieve high activity and selectivity has become a primary focus in this field. Furthermore, innovation in catalyst preparation, optimization of the activity and selectivity, as well as deeper understanding of mechanisms are crucial to further advancing H_2O_2 production in an environmentally benign manner more effectively. To date, carbon-based electrocatalysts have demonstrated remarkable progress, driven by advances in engineering strategies that have significantly improved their performance over traditional methods. In the following section, we will summarize and discuss the challenges and future perspectives in this research area (Fig. 17), including the rational design of carbon catalysts (*e.g.*, atomic level engineering, multiple-synergistic effects), advanced synthesis methods, *in situ* characterization techniques, and system-level device design considerations for industrial applications.

The catalytic activity of carbon-based materials still has significant potential for further improvement. Multiple synergistic modification strategies can be employed, including defect engineering (*e.g.*, creating vacancies and edge sites to promote O_2 adsorption), chemical doping (*e.g.*, introducing N, B, or S heteroatoms to tune their electronic structure), facet control (*e.g.*, exposing specific crystal planes with optimal *OOH intermediate binding energy), surface active site design (*e.g.*, atomically dispersed metal–N_4 moieties), interface engineering (*e.g.*, constructing hybrid metal oxide/carbon junctions to facilitate charge transfer), and microstructural modulation (*e.g.*, developing hierarchically porous architectures to improve mass transport). Although existing strategies have made notable progress in the electrosynthesis of H_2O_2, the precise control of defects and single-atomic sties in carbon materials requires further investigation to optimize the balance between the intrinsic activity and selectivity of active sites. To precisely engineer defects in carbon-based materials, several methodologies can be utilized: (1) plasma irradiation (Ar, N_2, or O_2) for controlled introduction of vacancies and edge defects; (2) mechanical exfoliation techniques such as ball-milling or ultrasonication to create strain-induced defects; and (3) pyrolysis of metal–organic frameworks (MOFs) to derive defect-rich carbon matrices with atomic-level precision. Moreover, to promote the mass transfer process, tailoring the morphology of the catalysts with well-designed 3D hierarchically porous architectures can significantly increase the availability of active sites and accelerate the diffusion of reactants. The pore sizes and distribution need to be carefully designed to balance the retention time and selective H_2O_2 production, reactant diffusion, resistance and reaction kinetics. Specific methods include the use of sacrificial templates (*e.g.*, mesoporous silica, PMMA spheres, and amphiphilic block copolymers), combination with resins (*e.g.*, resorcinol–formaldehyde) for ordered mesopores, or addition of macroporogen (*e.g.*, emulsion droplets) for triple

Open Access Article. Published on 21 April 2025. Downloaded on 6/16/2026 6:54:28 AM.
This article is licensed under a Creative Commons Attribution-NonCommercial 3.0 Unported Licence.

Table 2 Summary of representative carbon-based materials for electrocatalytic H_2O_2 production

Type	Catalysts	Electrolyte	Onset potential (V *vs.* RHE)	H_2O_2 selectivity (%)	Production rate	Voltage (V *vs.* RHE)	Faradaic efficiency (%)	Tafel slope (mV dec^{-1})	Stability	Ref.
Microstructure modulation	Carbon mesoporous nanoreactors (MHCS)	0.1 M KOH	0.6	85	3.36 mmol L^{-1} h^{-1}	0.5	97	73	12 h	83
	Graphitic ordered mesoporous carbon (O-GOMC)	0.1 M KOH	0.75	~92	63.33 mg L^{-1} h^{-1}	0.6	99.2	42	168 h	164
	O-GOMC	0.1 M KOH	0.73	93 ± 1	24 mmol L^{-1}	—	99	59	16 h (3 mA)	165
	Honeycomb carbon nanofibers (HCNFs)	0.1 M KOH	0.87	97.3	6.37 mmol L^{-1} h^{-1} (0.05 mg)	0.5	—	75.6	12 h	166
	Porous carbon (PCC_{900})	0.1 M KOH	0.83	95	1696.8 mmol g^{-1} h^{-1}	—	90	38	10 000 times	167
	Hollow mesoporous carbon spheres (HMCSs)	0.1 M KOH	0.82	95	—	0.53	87	—	10 h	168
	Mesoporous carbon-nanofibers (MCNF)	0.1 M KOH	0.68	>90	—	0.4	>85	43	12 h	98
	Holey graphene	0.1 M KOH	0.56	95	2360 mmol g^{-1} h^{-1}	0.1	97	—	12 h	169
Defect engineering	Oxidized carbon nanotubes	0.1 M KOH	0.795	>90	—	4	>85	38	96 h	170
	Oxygen-doped carbon quantum dots	0.1 M KOH	—	96.2	338.7 mmol g^{-1} h^{-1}	−1.33	92	66.95	120 h	171
	Oxygen modified defective graphene	0.1 M KOH	0.9	98.38	41.45 mg cm^{-2} h^{-1}	0.5	95	—	10	172
	Doped carbon nanohorns	0.1 M KOH	0.85	>80	740 mmol g^{-1} h^{-1}	0.65	50–100	49	12 h	173
	B-doped carbon	0.1 M KOH	0.780	88.7	24 300 mmol g^{-1} h^{-1}	—	82	51	100 h (100 mA cm^{-2})	161
	B-doped nanocarbon	0.1 M KOH	0.78	95	247 mg L^{-1} h^{-1}	0.5	100	—	10 h	174
	B-doped carbon	0.1 M KOH	0.773	95	7.36 mmol cm^{-2} h^{-1}	—	90	78	30 h (200 mA cm^{-2})	81
	N-doped carbon spheres	0.1 M KOH	0.7	91.9	618.5 mmol g^{-1} h^{-1}	0.4	85.1	—	10 h	90
	N-doped graphene	0.1 M KOH	0.764	>82	224.8 mmol g^{-1} h^{-1}	0.3	>43.6	—	4 h	175
	N-doped carbon	0.1 M $HClO_4$	0.6	80–98	2923 mg L^{-1} h^{-1}	0.3	100	136.6	10 h	176
	N-doped carbon	0.5 M NaCl	0.61	95	631.2 mmol g^{-1} h^{-1}	0.51	79.8	79	10 h	177
	N,O co-doped carbon nanosheets	0.1 M K_2SO_4	0.65	>90	6705 mmol g^{-1} h^{-1}	0.2	91	52	24 h	89
Surface modification	Polydopamine modified carbon (CB-PDA-A)	0.1 M KOH	0.8	80	1800 mmol g^{-1} h^{-1}	1.5	95	70	250 h	60
	CoPc-carbon	0.1 M KOH	0.7 V	99%	10 400 mmol g^{-1} h^{-1}	0.2	93	54	24 h	178
	Polymerization of acrylonitrile (PNAC-F)	0.1 M KOH	0.78	93	816 mmol g^{-1} h^{-1}	0.78	—	—	40 h	179
	Carbon black	0.1 M KOH	0.75	96	—	0.33	—	60	10 h	180
	Activated coke@carbon cloth	0.1 M Na_2SO_4	—	100	30.41 mg h^{-1} cm^{-2}	—	80	104.1	10 h	181
	N-B-OH-graphene quantum dots	0.1 M KOH	0.7	90	709 mmol g^{-1} h^{-1}	0.2	81	—	12 h	108
Single-atom—carbon hybrids	Pb-carbon dot (Pb SAs/OSC)	0.10 M KOH	0.65	>90	6.9 mmol cm^{-1} h^{-1}	—	92.7	49	100 h (50 mA cm^{-2})	144
	Single atoms cellulose-carbon (FeSAs/ACs-BCC)	0.1 M KOH	0.78	96.5	12 510 mmol g^{-1} h^{-1}	0.4	89.4	73	12 h	139
	In single atoms on carbon (In SAs/NSBC)	0.1 M KOH	0.66	95	6490 mmol g^{-1} h^{-1}	0.3	75	30.3	12 h	146
	Pt single atoms-g-C_3N_4 ($Pt_{0.21}$/CN)	0.1 M KOH	0.81	98	767 mmol g^{-1} h^{-1}	0.6	96	—	10 h	142
	Metal–nitrogen–carbon	0.1 M $HClO_4$	0.75	>70	688 mmol g^{-1} h^{-1}	0.3	93	113	12 h	182
Synergistic effects	CoZn–N/O-carbon nanotube ($CoZn_{SA}$@CNTs)	0.1 M KOH	—	90–100	4770 mmol g^{-1} h^{-1}	0.2	95	76.3	5 h	84
	Co–O_4 porous graphene-like carbon (Co–O_4@PC)	0.1 M KOH	0.73	98.8	250 mmol g^{-1} h^{-1}	0.5	—	72	10 h	137
	Co–N_4, C–O–C epoxide groups	0.1 M KOH	0.801	91.3	6912 mmol g^{-1} h^{-1}	0.09	—	51.3	10 h	135
	Atomic metal–nitrogen–carbon (F/Co–N–G SAC)	0.1 M KOH	0.810	94.2	12 100 mmol g^{-1} h^{-1}	0.1	70	45.2	10 h	183
	S,N-coordinated Ni SAC (Ni-N_3S)	0.1 M KOH	0.80	90.0	17 500 mmol g^{-1} h^{-1}	0.2	85	—	12 h	184
	Bipyridyl N-carbonyl (Pd-N_2O_2-C)	0.1 M KOH	0.82	95	1.5 × 107 mmol g^{-1} h^{-1}	0.4	—	—	10 h	185
	Pd atoms on nitrogen-doped carbon (Pd-NC)	0.1 M KOH	0.8	95	30 mmol g^{-1} h^{-1}	0.5	—	56	8 h	82
	Carbon-based single atom (Zn–N_2O_2–S SAC)	0.1 M KOH	—	96	6924 mmol g^{-1} h^{-1}	—	93.1	62	65 h (80 mA cm^{-2})	131
	Co SACs-carbon nanofiber (Co@EO-ACNF)	0.1 M KOH	—	85.21	15 750 mmol g^{-1} h^{-1}	0.6	84.5	—	48 h	136
	W SAC on O,N-doped carbon (W_1/NO-C)	0.1 M KOH	0.815	>90	1230 mmol g^{-1} h^{-1}	0.6	95	115	20 h	141
	Pd-oxidized carbon nanotubes	0.1 M $HClO_4$	0.7	95	1700 mmol g^{-1} h^{-1}	0.1	93	—	8 h	73
	Defective carbon (Mo-CDC-ns)	0.1 M KOH	0.75	90	455 mmol g^{-1} h^{-1}	0.55	85.1	95–99	12 h	100
	Co@carbon nanocages	0.1 M $HClO_4$	0.60	94	57 mmol g^{-1} h^{-1}	0.31	—	107.9	10 h	152
	Ni SAC-carboxyl-multiwall carbon nanotubes ($N_4Ni_1O_2$/OCNTs)	1 M KOH	0.68	—	5.7 mmol cm^{-2} h^{-1}	—	96.1	107	24 h (200 mA cm^{-2})	132
	Oxygen-vacancy-graphene armor (B/N-HCNS@V-G)	1 M KOH	0.79	91	55 ppm	0.5	94	63	24 h	115
	Carbon nanotubes with N,S-rich tips (N, S-TCNTs)	1 M KOH	0.78	90.0	30 370 mmol g^{-1} h^{-1}	—	>90	55.5	200 h (100 mA)	160

This journal is © The Royal Society of Chemistry 2025

Open Access Article. Published on 21 April 2025. Downloaded on 6/16/2026 6:54:28 AM.
This article is licensed under a Creative Commons Attribution-NonCommercial 3.0 Unported Licence.

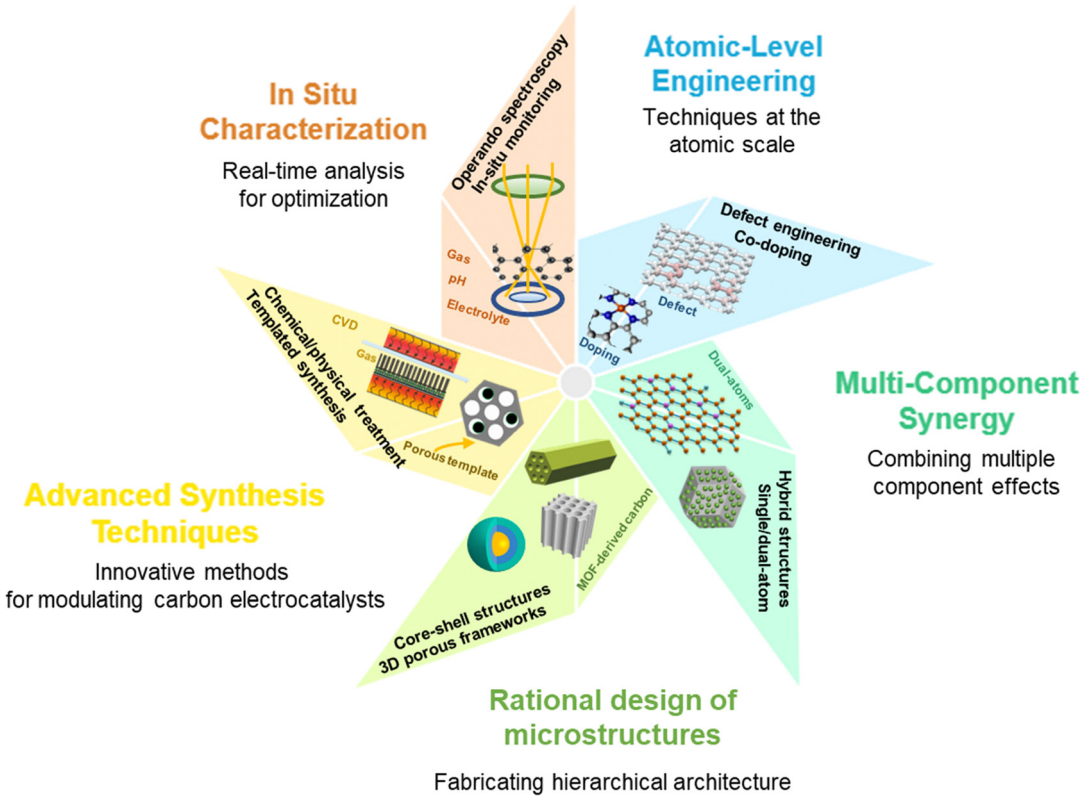

Fig. 17 Schematic of perspective strategizes for rational design of carbon catalysts (atomic level engineering, multiple-synergistic effects), advanced synthesis method, and *in situ* characterization techniques.

porosity. In addition, it is crucial to introduce surface functional groups (*e.g.*, –COOH or –OH) to tune hydrophilicity for improving electrolyte accessibility and modifying intermediate binding strength through dipole interactions. For single-atom carbon catalysts, the uncontrollable selectivity and poor stability remain critical challenges. The implementation of atomic layer deposition (ALD) for depositing protective layer (*e.g.*, Al_2O_3 or TiO_2 sub-nanolayers) can be used to enhance the stability while allowing reactant access; creating proximal dual-atom sites is effective to promote the selectivity by modulating the O–O bond cleavage. Critically, the synergistic integration of these strategies represents a pivotal research direction for achieving sustained high selectivity in the $2e^-$ oxygen reduction pathway. Beyond catalyst design, the role of the electrolyte in H_2O_2 production also deserves attention, as it can influence the stability of the key intermediate *OOH, thereby regulating the overall efficiency of H_2O_2 formation. And the ORR activity through the $2e^-$ pathway remains limited for many carbon-based materials in neutral or weakly acidic environments.

Beyond materials design, elucidating the fundamental electrocatalytic mechanisms remains a critical research priority. At this moment, the reaction mechanisms of carbon-based electrocatalysts remain insufficiently understood. It is worth noting that the active sites in carbon catalysts typically undergo dynamic evolution during electrochemical reactions, necessitating the study of these changes to fully explore the reaction mechanisms. To this end, a comprehensive understanding of reaction pathways, active site dynamics under operational conditions, and interfacial phenomena is essential for rationally guiding catalyst optimization. Therefore, various *in situ*/*operando* characterization techniques are needed to directly probe reactive intermediates, active sites, and their interactions during the electrochemical H_2O_2 generation process. For instance, *in situ* XRD and X-ray absorption spectroscopy (XAS) can be employed to analyze the local coordination environment, electronic structure, and oxidation state of catalysts in real time. In addition, *in situ* Raman and FTIR spectroscopy are valuable for real-time detection of reaction intermediates during electrocatalysis reactions. Further improvement in spatial and temporal resolution for *in situ* detection of dynamic electrocatalytic processes is also desirable. To gain deeper insights into electrocatalytic mechanisms, advanced theoretical calculations are needed to quantitatively correlate the energetics of intermediates with reaction kinetics. With ongoing advances in computational power, algorithms, and big data from both experiments and simulations, machine learning could play a transformative role in predicting structure–performance relationships at previously unattainable scales. At present, the $2e^-$ WOR has received less attention and is in its early stages of development compared to the $2e^-$ ORR. Thus, the development of novel computational approaches to screen and guide the design of advanced carbon-based $2e^-$ WOR electrocatalysts is essential. A fundamental mechanistic understanding will elucidate the critical interplay between: (1) reaction intermediate energetics, (2) surface-dependent selectivity determinants (*e.g.*, *OOH binding strength, local coordination environments), and (3) electrochemical

Open Access Article. Published on 21 April 2025. Downloaded on 6/16/2026 6:54:28 AM. This article is licensed under a Creative Commons Attribution-NonCommercial 3.0 Unported Licence.

microenvironment effects (pH, potential, double-layer structure), ultimately enabling rational design of efficient H_2O_2 production systems.

While catalyst design has advanced significantly, it is worth noting that the development of electrochemical reactors has lagged behind catalyst design in the past decade. Therefore, system-level optimization is essential for practical implementation of carbon-based electrocatalysts. Particular emphasis should be placed on the design of the overall electrochemical system and the operational reliability of the industrial-grade device for practical applications. Key considerations include O_2 mass transfer, device design, electrolyte selection, ion exchange membranes, and reactor configurations. First, the mass transfer and diffusion of reactant species within the interface microenvironment of the carbon electrode needs further investigation.[181] Specific optimization strategies involve gas diffusion electrodes with hierarchical porosity (macro/meso/micro pores) to balance O_2 transport and flow-through membrane reactors with rotational cathodes. The use of a porous solid electrolyte (PSE) reactor for producing high-concentration and high-purity H_2O_2 may meet the high stability requirment.[186] In addition, optimizing local reaction environments—such as water permeation/wetting, hydrophobicity/hydrophilicity, and reactant concentration—can enhance the performance of carbon-based electrocatalysts. Significant research efforts should focus on advancing reactor engineering, particularly for flow cell configurations and dual-PEM solid electrolyte systems. These reactor designs must simultaneously address two critical challenges: (1) corrosion resistance against both acidic/alkaline electrolytes and concentrated H_2O_2 (up to 10 wt%), and (2) maintenance of stable three-phase interfaces under industrial current densities (>200 mA cm^{-2}). Innovative architectures incorporating corrosion-resistant materials (*e.g.*, PTFE-coated titanium flow fields, stabilized carbon-PTFE gas diffusion electrodes) and optimized hydrodynamics are crucial for achieving economically viable H_2O_2 electrosynthesis on a large scale. Furthermore, the H_2O_2 products are typically generated in a mixture, with solutes in traditional liquid electrolytes ranging from acidic to alkaline pH. Extra separation processes to recover pure H_2O_2 solutions are therefore required. Using a solid-state electrolyte can avoid contamination of the product solution by extraneous ions.[2] Producing H_2O_2 in neutral solutions offers practical advantages by avoiding pH-related complications, such as electrode degradation or the need for neutralization steps. Seawater, as an abundant and naturally neutral electrolyte, directly supports this goal by providing a sustainable medium for electrochemical H_2O_2 production *via* the $2e^-$ ORR pathway. The dissolved oxygen serves as a reactant for carbon-based electrocatalysts, which have demonstrated high efficacy in neutral media. Moreover, the use of seawater eliminates the costs and environmental impacts associated with synthetic pH adjustments, enhancing both scalability and the sustainability of the process. However, challenges such as chloride interference may compromise catalyst stability and selectivity, necessitating the development of robust carbon-based materials and more in-depth mechanistic studies in simulated seawater electrolytes to fully realize these benefits. Consequently, exploring suitable and stable carbon-based catalysts and understanding the catalytic mechanism in neutral simulated seawater electrolytes are urgent and promising areas of research.[187] Moreover, sustainable H_2O_2 production coupled with the high value added chemical synthesis is worth exploring, such as oxidative valorization of glycerol[188] and upgrading of cellulosic biomass into valued formic acid.[189]

Data availability

No new experimental data were generated in this study. All data supporting the findings of this review are available in the cited literature and references within the manuscript.

Conflicts of interest

There are no conflicts to declare.

Acknowledgements

This work was supported by financial aid from the National Natural Science Foundation of China (Grant No. 22075126, 52202242 and 52172187), the Ministry of Human Resources and Social Security of China (H20240006), the Start-up funding for Jinshan Distinguished Professor of Jiangsu University, and the Jiangsu Provincial Senior Talent Program (Dengfeng).

References

1 R. Ciriminna, L. Albanese, F. Meneguzzo and M. Pagliaro, *ChemSusChem*, 2016, **9**, 3374–3381.
2 S. C. Perry, D. Pangotra, L. Vieira, L.-I. Csepei, V. Sieber, L. Wang, C. Ponce de León and F. C. Walsh, *Nat. Rev. Chem.*, 2019, **3**, 442–458.
3 J. A. Dowling, K. Z. Rinaldi, T. H. Ruggles, S. J. Davis, M. Yuan, F. Tong, N. S. Lewis and K. Caldeira, *Joule*, 2020, **4**, 1907–1928.
4 O. C. Esan, X. Shi, Z. Pan, Y. Liu, X. Huo, L. An and T. S. Zhao, *J. Power Sources*, 2022, **548**, 232114.
5 J. M. Campos-Martin, G. Blanco-Brieva and J. L. G. Fierro, *Angew. Chem., Int. Ed.*, 2006, **45**, 6962–6984.
6 A. G. Fink, R. S. Delima, A. R. Rousseau, C. Hunt, N. E. LeSage, A. Huang, M. Stolar and C. P. Berlinguette, *Nat. Commun.*, 2024, **15**, 766.
7 S. J. Freakley, Q. He, J. H. Harrhy, L. Lu, D. A. Crole, D. J. Morgan, E. N. Ntainjua, J. K. Edwards, A. F. Carley, A. Y. Borisevich, C. J. Kiely and G. J. Hutchings, *Science*, 2016, **351**, 965–968.
8 T. Ricciardulli, S. Gorthy, J. S. Adams, C. Thompson, A. M. Karim, M. Neurock and D. W. Flaherty, *J. Am. Chem. Soc.*, 2021, **143**, 5445–5464.
9 Y. Zhang, C. Pan, G. Bian, J. Xu, Y. Dong, Y. Zhang, Y. Lou, W. Liu and Y. Zhu, *Nat. Energy*, 2023, **8**, 361–371.
10 R. Liu, Y. Chen, H. Yu, M. Položij, Y. Guo, T. C. Sum, T. Heine and D. Jiang, *Nat. Catal.*, 2024, **7**, 195–206.

 This journal is © The Royal Society of Chemistry 2025

Open Access Article. Published on 21 April 2025. Downloaded on 6/16/2026 6:54:28 AM. This article is licensed under a Creative Commons Attribution-NonCommercial 3.0 Unported Licence.

11 Z. Teng, Q. Zhang, H. Yang, K. Kato, W. Yang, Y.-R. Lu, S. Liu, C. Wang, A. Yamakata, C. Su, B. Liu and T. Ohno, *Nat. Catal.*, 2021, **4**, 374–384.
12 H. Tan, P. Zhou, M. Liu, Q. Zhang, F. Liu, H. Guo, Y. Zhou, Y. Chen, L. Zeng, L. Gu, Z. Zheng, M. Tong and S. Guo, *Nat. Synth.*, 2023, **2**, 557–563.
13 Y. Shiraishi, T. Takii, T. Hagi, S. Mori, Y. Kofuji, Y. Kitagawa, S. Tanaka, S. Ichikawa and T. Hirai, *Nat. Mater.*, 2019, **18**, 985–993.
14 R. Pan, W. Lv, X. Ge, X. Huang, Q. Hu, K. Song, Q. Liu, H. Xie, B. Wu and J. Yuan, *Adv. Funct. Mater.*, 2025, **35**, 2414193.
15 Y. Liu, L. Li, Z. Sang, H. Tan, N. Ye, C. Sun, Z. Sun, M. Luo and S. Guo, *Nat. Synth.*, 2025, **4**, 134–141.
16 P. Sun, Z. Mo, J. Zhang, G. Wu, Z. Miao, K. Zhong, Y. Wei, C. Jia, Z. Chen and H. Xu, *Chem. Eng. J.*, 2023, **478**, 147337.
17 H. Jiang, L. Wang, X. Yu, L. Sun, J. Li, J. Yang and Q. Liu, *Chem. Eng. J.*, 2023, **466**, 143129.
18 C. Zhou, Y. Song, Z. Wang, J. Liu, P. Sun, Z. Mo, J. Yi and L. Zhai, *J. Environ. Chem. Eng.*, 2023, **11**, 110138.
19 W. Wang, L. Wang, L. Sun, H. Jiang, Y. Liu, Q. Liu, X. She and H. Tang, *Chem. Eng. J.*, 2023, **477**, 146945.
20 R. Chen, Z. Zhang, J. Wu, X. Chen, L. Wang, H. Yin, H. Li, J. Ding, H. Wan and G. Guan, *Renewable Energy*, 2022, **197**, 943–952.
21 Z. Lu, G. Chen, S. Siahrostami, Z. Chen, K. Liu, J. Xie, L. Liao, T. Wu, D. Lin, Y. Liu, T. F. Jaramillo, J. K. Nørskov and Y. Cui, *Nat. Catal.*, 2018, **1**, 156–162.
22 C. Xia, Y. Xia, P. Zhu, L. Fan and H. Wang, *Science*, 2019, **366**, 226–231.
23 E. Jung, H. Shin, B.-H. Lee, V. Efremov, S. Lee, H. S. Lee, J. Kim, W. Hooch Antink, S. Park, K.-S. Lee, S.-P. Cho, J. S. Yoo, Y.-E. Sung and T. Hyeon, *Nat. Mater.*, 2020, **19**, 436–442.
24 S. Siahrostami, A. Verdaguer-Casadevall, M. Karamad, D. Deiana, P. Malacrida, B. Wickman, M. Escudero-Escribano, E. A. Paoli, R. Frydendal, T. W. Hansen, I. Chorkendorff, I. E. L. Stephens and J. Rossmeisl, *Nat. Mater.*, 2013, **12**, 1137–1143.
25 Y. Jiang, P. Ni, C. Chen, Y. Lu, P. Yang, B. Kong, A. Fisher and X. Wang, *Adv. Energy Mater.*, 2018, **8**, 1801909.
26 X. Sun, J. Yang, X. Zeng, L. Guo, C. Bie, Z. Wang, K. Sun, A. K. Sahu, M. Tebyetekerwa, T. E. Rufford and X. Zhang, *Angew. Chem., Int. Ed.*, 2024, **63**, e202414417.
27 D. Deng, J. Wang, M. Wang, Y. Wang, J. Jiang, Y. Chen, Y. Bai, Q. Wu and Y. Lei, *J. Mater. Sci. Technol.*, 2025, **227**, 76–81.
28 L. Cui, B. Chen, D. Chen, C. He, Y. Liu, H. Zhang, J. Qiu, L. Liu, W. Jing and Z. Zhang, *Nat. Commun.*, 2024, **15**, 10632.
29 J. Zhao, X. Zhang, J. Xu, W. Tang, Z. Lin Wang and F. Ru Fan, *Angew. Chem., Int. Ed.*, 2023, **62**, e202300604.
30 M. Ran, B. Du, W. Liu, Z. Liang, L. Liang, Y. Zhang, L. Zeng and M. Xing, *Proc. Natl. Acad. Sci. U. S. A.*, 2024, **121**, e2317435121.
31 S. Li, X. Zhang, F. Yang, J. Zhang, W. Shi and F. Rosei, *Chem. Catal.*, 2024, **4**, 100901.
32 S. Li, X. Liu, X. Zhang and Y. Liu, *Catalysts*, 2025, **15**, 157.
33 S. Li, X. Liu, X. Zhang, Y. Wang, S. Chen, Y. Liu and Y. Zhang, *Catalysts*, 2024, **14**, 159.
34 Q. Yang, Y. Gu, Y. Liu, X. Wang, S. Li, J. Zhang, W. Liu, L. Zhang and Y. Zhang, *Chem. Commun.*, 2024, **60**, 13554–13557.
35 Y. Zhang, S. Li, J. Zhang, L.-D. Zhao, Y. Lin, W. Liu and F. Rosei, *Natl. Sci. Rev.*, 2024, **11**, nwae036.
36 S. Yang, A. Verdaguer-Casadevall, L. Arnarson, L. Silvioli, V. Čolić, R. Frydendal, J. Rossmeisl, I. Chorkendorff and I. E. L. Stephens, *ACS Catal.*, 2018, **8**, 4064–4081.
37 S. Siahrostami, S. J. Villegas, A. H. Bagherzadeh Mostaghimi, S. Back, A. B. Farimani, H. Wang, K. A. Persson and J. Montoya, *ACS Catal.*, 2020, **10**, 7495–7511.
38 J. Wang, D. Kim, J. H. Park, S. Ryu, M. Shokouhimehr and H. W. Jang, *Energy Fuels*, 2023, **37**, 17629–17651.
39 A. Yu, S. Liu and Y. Yang, *Chem. Commun.*, 2024, **60**, 5232–5244.
40 Y. Wang, G. I. N. Waterhouse, L. Shang and T. Zhang, *Adv. Energy Mater.*, 2021, **11**, 2003323.
41 J. S. Jirkovský, I. Panas, E. Ahlberg, M. Halasa, S. Romani and D. J. Schiffrin, *J. Am. Chem. Soc.*, 2011, **133**, 19432–19441.
42 K. Gong, F. Du, Z. Xia, M. Durstock and L. Dai, *Science*, 2009, **323**, 760–764.
43 Q. Zhai, H. Huang, T. Lawson, Z. Xia, P. Giusto, M. Antonietti, M. Jaroniec, M. Chhowalla, J.-B. Baek, Y. Liu, S. Qiao and L. Dai, *Adv. Mater.*, 2024, **36**, 2405664.
44 H. W. Kim, M. B. Ross, N. Kornienko, L. Zhang, J. Guo, P. Yang and B. D. McCloskey, *Nat. Catal.*, 2018, **1**, 282–290.
45 J. Zhu, X. Xiao, K. Zheng, F. Li, G. Ma, H.-C. Yao, X. Wang and Y. Chen, *Carbon*, 2019, **153**, 6–11.
46 M. Niamlaem, C. Boonyuen, W. Sangthong, J. Limtrakul, D. Zigah, A. Kuhn and C. Warakulwit, *Carbon*, 2020, **170**, 154–164.
47 J. Biemolt, K. van der Veen, N. J. Geels, G. Rothenberg and N. Yan, *Carbon*, 2019, **155**, 643–649.
48 T.-N. Pham-Truong, T. Petenzi, C. Ranjan, H. Randriamahazaka and J. Ghilane, *Carbon*, 2018, **130**, 544–552.
49 A. R. Puente Santiago, O. Fernandez-Delgado, A. Gomez, M. A. Ahsan and L. Echegoyen, *Angew. Chem., Int. Ed.*, 2021, **60**, 122–141.
50 Y. Liu, X. Quan, X. Fan, H. Wang and S. Chen, *Angew. Chem., Int. Ed.*, 2015, **54**, 6837–6841.
51 L. Jing, W. Wang, Q. Tian, Y. Kong, X. Ye, H. Yang, Q. Hu and C. He, *Angew. Chem., Int. Ed.*, 2024, **63**, e202403023.
52 J. S. Lim, J. H. Kim, J. Woo, D. S. Baek, K. Ihm, T. J. Shin, Y. J. Sa and S. H. Joo, *Chem*, 2021, **7**, 3114–3130.
53 L. Wei, Z. Dong, R. Chen, Q. Wu and J. Li, *Ionics*, 2022, **28**, 4045–4063.
54 Z.-y Sang, F. Hou, S.-H. Wang and J. Liang, *Carbon*, 2022, **192**, 484.
55 Y.-Y. Yan, W.-J. Niu, W.-W. Zhao, R.-J. Li, E.-P. Feng, B.-X. Yu, B.-K. Chu and C.-Y. Cai, *Adv. Energy Mater.*, 2024, **14**, 2303506.
56 H. He, S. Liu, Y. Liu, L. Zhou, H. Wen, R. Shen, H. Zhang, X. Guo, J. Jiang and B. Li, *Green Chem.*, 2023, **25**, 9501–9542.
57 Z. Deng, S. J. Choi, G. Li and X. Wang, *Chem. Soc. Rev.*, 2024, **53**, 8137–8181.
58 X. Shi, S. Siahrostami, G.-L. Li, Y. Zhang, P. Chakthranont, F. Studt, T. F. Jaramillo, X. Zheng and J. K. Nørskov, *Nat. Commun.*, 2017, **8**, 701.

Open Access Article. Published on 21 April 2025. Downloaded on 6/16/2026 6:54:28 AM. This article is licensed under a Creative Commons Attribution-NonCommercial 3.0 Unported Licence.

59 L. Lin, L. Huang, C. Wu, Y. Gao, N. Miao, C. Wu, A. T. Marshall, Y. Zhao, J. Wang, J. Chen, S. Dou, G. G. Wallace and W. Huang, *Angew. Chem., Int. Ed.*, 2023, **62**, e202315182.
60 J. Su, L. Jiang, B. Xiao, Z. Liu, H. Wang, Y. Zhu, J. Wang and X. Zhu, *Small*, 2023, **20**, 2310317.
61 R. Xie, C. Cheng, R. Wang, J. Li, E. Zhao, Y. Zhao, Y. Liu, J. Guo, P. Yin and T. Ling, *ACS Catal.*, 2024, **14**, 4471–4477.
62 X. Luo, R. Zhu, L. Zhao, X. Gong, L. Zhang, L. Fan and Y. Liu, *Environ. Res.*, 2024, **251**, 118644.
63 S. Luo, K. Elouarzaki and Z. J. Xu, Electrochemistry in Magnetic Fields, *Angew. Chem., Int. Ed.*, 2022, **61**, e202203564.
64 X. Hu, Z. Sun, G. Mei, X. Zhao, B. Y. Xia and B. You, *Adv. Energy Mater.*, 2022, **12**, 2201466.
65 D. Kai, L. Jie, W. Yuanyuan, R. Yuchun, X. Zhaoquan, Z. Haiping, L. Lei, L. Qian, L. Yonglan, L. Tingshuai, M. A. Abdullah, L. Quan, M. Dongwei and S. Xuping, *Chem. Catal.*, 2021, **1**, 1437–1448.
66 S. Mavrikis, M. Göltz, S. C. Perry, F. Bogdan, P. K. Leung, S. Rosiwal, L. Wang and C. Ponce de León, *ACS Energy Lett.*, 2021, **6**, 2369–2377.
67 Z. Chen, X. Liu, K. Wang, L. Yang, Y. Wang, X. Wang, S. Song and Z. Chen, *Adv. Funct. Mater.*, 2025, **35**, 2413243.
68 Y. Liang, Y. Han, J.-S. Li, J. Wang, J. D. Liu and Q. Fan, *J. Energy Chem.*, 2022, **70**, 643–655.
69 Y. Wang and Y. Xue, *ACS Appl. Nano Mater.*, 2023, **6**, 23565–23575.
70 H. Zhang, Y. Zhao, Y. Li, G. Li, J. Li and F. Zhang, *ACS Appl. Energy Mater.*, 2020, **3**, 705–714.
71 S. Sun, J. Dang, K. Ji, Z. Shi, M. Chen, C. Zhang and S. Liu, *Renewable Sustainable Energy Rev.*, 2023, **183**, 113538.
72 Y. Jia and X. Yao, *Chem*, 2020, **6**, 548–550.
73 Q. Chang, P. Zhang, A. H. B. Mostaghimi, X. Zhao, S. R. Denny, J. H. Lee, H. Gao, Y. Zhang, H. L. Xin, S. Siahrostami, J. G. Chen and Z. Chen, *Nat. Commun.*, 2020, **11**, 2178.
74 F. Y. Yu, Y. J. Zhou, H. Q. Tan, Y. G. Li and Z. H. Kang, *Adv. Energy Mater.*, 2023, **13**, 2300119.
75 M. Deng, D. Wang and Y. Li, *Adv. Mater.*, 2024, **36**, 2314340.
76 N. Ramaswamy, U. Tylus, Q. Jia and S. Mukerjee, *J. Am. Chem. Soc.*, 2013, **135**, 15443–15449.
77 N. Ramaswamy and S. Mukerjee, *Phys. Chem. C*, 2011, **115**, 18015–18026.
78 Y. Tang, B. L. Allen, D. R. Kauffman and A. Star, *J. Am. Chem. Soc.*, 2009, **131**, 13200–13201.
79 T.-P. Fellinger, F. Hasché, P. Strasser and M. Antonietti, *J. Am. Chem. Soc.*, 2012, **134**, 4072–4075.
80 Y. Pang, K. Wang, H. Xie, Y. Sun, M.-M. Titirici and G.-L. Chai, *ACS Catal.*, 2020, **10**, 7434–7442.
81 Y. Xia, X. Zhao, C. Xia, Z.-Y. Wu, P. Zhu, J. Y. Kim, X. Bai, G. Gao, Y. Hu, J. Zhong, Y. Liu and H. Wang, *Nat. Commun.*, 2021, **12**, 4225.
82 N. Wang, X. Zhao, R. Zhang, S. Yu, Z. H. Levell, C. Wang, S. Ma, P. Zou, L. Han, J. Qin, L. Ma, Y. Liu and H. L. Xin, *ACS Catal.*, 2022, **12**, 4156–4164.
83 Q. Tian, L. Jing, H. Du, Y. Yin, X. Cheng, J. Xu, J. Chen, Z. Liu, J. Wan, J. Liu and J. Yang, *Nat. Commun.*, 2024, **15**, 983.
84 L. Yang, H. Cheng, H. Li, G. Sun, S. Liu, T. Ma and L. Zhang, *Adv. Mater.*, 2024, **36**, 2406957.
85 Q. Tian, L. Jing, Y. Yin, Z. Liang, H. Du, L. Yang, X. Cheng, D. Zuo, C. Tang, Z. Liu, J. Liu, J. Wan and J. Yang, *Nano Lett.*, 2024, **24**, 1650–1659.
86 C. Du, P. Li, Z. Zhuang, Z. Fang, S. He, L. Feng and W. Chen, *Coord. Chem. Rev.*, 2022, **466**, 214604.
87 L. Kořená, V. Slovák, G. Zelenková and T. Zelenka, *Carbon*, 2023, **206**, 303–313.
88 A. Wang, Y. Ma and D. Zhao, *ACS Nano*, 2024, **18**, 22829–22854.
89 L. Jing, Q. Tian, W. Wang, X. Li, Q. Hu, H. Yang and C. He, *Adv. Energy Mater.*, 2024, **14**, 2304418.
90 Y. Hu, J. Zhang, T. Shen, Z. Li, K. Chen, Y. Lu, J. Zhang and D. Wang, *ACS Appl. Mater. Interfaces*, 2021, **13**, 29551–29557.
91 J. Xi, S. Yang, L. Silvioli, S. Cao, P. Liu, Q. Chen, Y. Zhao, H. Sun, J. N. Hansen, J.-P. B. Haraldsted, J. Kibsgaard, J. Rossmeisl, S. Bals, S. Wang and I. Chorkendorff, *J. Catal.*, 2021, **393**, 313–323.
92 C. Qi, W. Bao, J. Xu, Y. Li, F. Xu, M. Li, L. Wang, W. Jiang, P. Qiu and W. Luo, *Angew. Chem., Int. Ed.*, 2025, **64**, e202500177.
93 W. Zhu, Z. Chen, Y. Pan, R. Dai, Y. Wu, Z. Zhuang, D. Wang, Q. Peng, C. Chen and Y. Li, *Adv. Mater.*, 2019, **31**, 1800426.
94 Z. Yu, N. Ji, X. Li, R. Zhang, Y. Qiao, J. Xiong, J. Liu and X. Lu, *Angew. Chem., Int. Ed.*, 2023, **62**, e202213612.
95 X. Tang, Y. Wei, W. Zhai, Y. Wu, T. Hu, K. Yuan and Y. Chen, *Adv. Mater.*, 2023, **35**, 2208942.
96 Y. Bu, Y. Wang, G.-F. Han, Y. Zhao, X. Ge, F. Li, Z. Zhang, Q. Zhong and J.-B. Baek, *Adv. Mater.*, 2021, **33**, 2103266.
97 J. Zhu and S. Mu, *Adv. Funct. Mater.*, 2020, **30**, 2001097.
98 L. Jing, Q. Tian, X. Li, J. Sun, W. Wang, H. Yang, X. Chai, Q. Hu and C. He, *Adv. Funct. Mater.*, 2023, **33**, 2305795.
99 Z. Mou, Y. Mu, L. Liu, D. Cao, S. Chen, W. Yan, H. Zhou, T.-S. Chan, L.-Y. Chang and X. Fan, *Small*, 2024, **20**, 2400564.
100 C. Zhang, C. Wu, L. Wang and G. Liu, *ACS Appl. Mater. Interfaces*, 2023, **15**, 838–847.
101 J. Zhu, Y. Huang, W. Mei, C. Zhao, C. Zhang, J. Zhang, I. S. Amiinu and S. Mu, *Angew. Chem., Int. Ed.*, 2019, **58**, 3859–3864.
102 C. Zhang, W. Shen, K. Guo, M. Xiong, J. Zhang and X. Lu, *J. Am. Chem. Soc.*, 2023, **145**, 11589–11598.
103 D. San Roman, D. Krishnamurthy, R. Garg, H. Hafiz, M. Lamparski, N. T. Nuhfer, V. Meunier, V. Viswanathan and T. Cohen-Karni, *ACS Catal.*, 2020, **10**, 1993–2008.
104 Y. J. Sa, J. H. Kim and S. H. Joo, *Angew. Chem., Int. Ed.*, 2019, **58**, 1100–1105.
105 F. She, Z. Guo, F. Liu, Z. Yu, J. Chen, Y. Fan, Y. Lei, Y. Chen, H. Li and L. Wei, *ACS Catal.*, 2024, **14**, 10928–10938.
106 X. Wang, C. Han, Y. Han, R. Huang, H. Sun, P. Guo, X. Liu, M. Huang, Y. Chen, H. Wu, J. Zhang, X. Yan, Z. Mao, A. Du, Y. Jia and L. Wang, *Small*, 2024, **20**, 2401447.
107 W. Shen, C. Zhang, M. Alomar, Z. Du, Z. Yang, J. Wang, G. Xu, J. Zhang, J. Lv and X. Lu, *Nano Res.*, 2024, **17**, 1217–1224.
108 M. Fan, Z. Wang, K. Sun, A. Wang, Y. Zhao, Q. Yuan, R. Wang, J. Raj, J. Wu, J. Jiang and L. Wang, *Adv. Mater.*, 2023, **35**, 2209086.

 This journal is © The Royal Society of Chemistry 2025

Open Access Article. Published on 21 April 2025. Downloaded on 6/16/2026 6:54:28 AM. This article is licensed under a Creative Commons Attribution-NonCommercial 3.0 Unported Licence.

109 J. W. Choi, A. Byeon, S. Kim, C.-K. Hwang, W. Zhang, J. Lee, W. C. Yun, S. Y. Paek, J. H. Kim, G. Jeong, S. Y. Lee, J. Moon, S. S. Han, J. W. Lee and J. M. Kim, *Adv. Mater.*, 2025, **37**, 2415712, DOI: **10.1002/adma.202415712**.
110 N. Wang, S. Ma, R. Zhang, L. Wang, Y. Wang, L. Yang, J. Li, F. Guan, J. Duan and B. Hou, *Adv. Sci.*, 2023, **10**, 2302446.
111 Z. Xing, K. Shi, Z. S. Parsons and X. Feng, *ACS Catal.*, 2023, **13**, 2780–2789.
112 L. Xie, C. Liang, Y. Wu, K. Wang, W. Hou, H. Guo, Z. Wang, Y. M. Lam, Z. Liu and L. Wang, *Small*, 2024, **20**, 2401253.
113 W. Shen, C. Zhang, X. Wang, Y. Huang, Z. Du, M. Alomar, J. Wang, J. Lv, J. Zhang and X. Lu, *ACS Mater. Lett.*, 2024, **6**, 17–26.
114 H. Jiang, Y. Wang, J. Hao, Y. Liu, W. Li and J. Li, *Carbon*, 2017, **122**, 64–73.
115 Y. Wu, Z. Gao, Y. Feng, Q. Cui, C. Du, C. Yu, L. Liang, W. Zhao, J. Feng, J. Sun, R. Yang and J. Sun, *Appl. Catal., B*, 2021, **298**, 120572.
116 C. Ma, Q. Hao, J. Hou, A. Liu and X. Xiang, *Carbon Res.*, 2024, **3**, 5.
117 G.-F. Han, F. Li, W. Zou, M. Karamad, J.-P. Jeon, S.-W. Kim, S.-J. Kim, Y. Bu, Z. Fu, Y. Lu, S. Siahrostami and J.-B. Baek, *Nat. Commun.*, 2020, **11**, 2209.
118 X. Shen, Z. Wang, H. Guo, Z. Lei, Z. Liu and L. Wang, *Small*, 2023, **19**, 2303156.
119 Q. Wu, H. Zou, X. Mao, J. He, Y. Shi, S. Chen, X. Yan, L. Wu, C. Lang, B. Zhang, L. Song, X. Wang, A. Du, Q. Li, Y. Jia, J. Chen and X. Yao, *Nat. Commun.*, 2023, **14**, 6275.
120 J. Qu, G. Long, L. Luo, Y. Yang, W. Fan and F. Zhang, *Small*, 2024, **20**, 2400695.
121 X. Wen, X. Zhang, M. Wang, C. Yuan, J. Lang, X. Li, H. Wei, D. Mandler and M. Long, *Appl. Catal., B*, 2024, **342**, 123437.
122 G. Alemany-Molina, J. Fernández-Catalá, W. Cao, E. Morallón and D. Cazorla-Amorós, *Mater. Today Chem.*, 2024, **35**, 101858.
123 A. Zhang, Y. Liu, J. Wu, J. Zhu, S. Cheng, Y. Wang, Y. Hao and S. Zeng, *Chem. Eng. J.*, 2023, **454**, 140317.
124 A. B. Trench, J. Paulo, C. Moura, V. S. Antonin, C. Machado Fernandes, L. Liu and M. C. Santos, *Adv. Powder Technol.*, 2024, **35**, 104404.
125 M. A. Rashed, M. Faisal, F. A. Harraz, M. Jalalah, M. Alsaiari and S. A. Alsareii, *J. Electrochem. Soc.*, 2021, **168**, 027512.
126 B. Yu, J. Diniz, K. Lofgren, Q. Liu, R. Mercado, F. Nichols, S. R. J. Oliver and S. Chen, *ACS Sustain. Chem. Eng.*, 2022, **10**, 15501–15507.
127 C. Guo, Y. Ruan, S. Zhang, L. Kan, H. Bian, F. Rong, L. He, D. Li, M. Du and Z. Zhang, *Chem. Eng. J.*, 2023, **466**, 143033.
128 N. Cheng, S. Stambula, D. Wang, M. N. Banis, J. Liu, A. Riese, B. Xiao, R. Li, T.-K. Sham, L.-M. Liu, G. A. Botton and X. Sun, *Nat. Commun.*, 2016, **7**, 13638.
129 Q. Chang, P. Zhang, A. H. B. Mostaghimi, X. Zhao, S. R. Denny, J. H. Lee, H. Gao, Y. Zhang, H. L. Xin, S. Siahrostami, J. G. Chen and Z. Chen, *Nat. Commun.*, 2020, **11**, 2178.
130 C. Jing, J. Ding, P. Jia, M. Jin, L. Zhou, X. Liu, J. Luo and S. Dai, *Carbon Energy*, 2024, **6**, e581.
131 G. Wei, Y. Li, X. Liu, J. Huang, M. Liu, D. Luan, S. Gao and X. W. Lou, *Angew. Chem., Int. Ed.*, 2023, **62**, e202313914.
132 C. Xiao, L. Cheng, Y. Zhu, G. Wang, L. Chen, Y. Wang, R. Chen, Y. Li and C. Li, *Angew. Chem., Int. Ed.*, 2022, **61**, e202206544.
133 Y.-X. Du, Q. Yang, W.-T. Lu, Q.-Y. Guan, F.-F. Cao and G. Zhang, *Adv. Funct. Mater.*, 2023, **33**, 2300895.
134 M. Song, W. Liu, J. Zhang, C. Zhang, X. Huang and D. Wang, *Adv. Funct. Mater.*, 2023, **33**, 2212087.
135 H. Gong, Z. Wei, Z. Gong, J. Liu, G. Ye, M. Yan, J. Dong, C. Allen, J. Liu, K. Huang, R. Liu, G. He, S. Zhao and H. Fei, *Adv. Funct. Mater.*, 2022, **32**, 2106886.
136 C.-K. Hwang, S. Kim, K. R. Yoon, T. T. Le, C. V. Hoang, J. W. Choi, W. Zhang, S. Y. Paek, C. H. Lee, J. H. Lee, K. H. Chae, S. Jeong, S. Y. Lee, B.-K. Ju, S. H. Kim, S. S. Han and J. M. Kim, *Carbon Energy*, 2024, **6**, e582.
137 S. Zhang, Z. Tao, M. Xu, L. Kan, C. Guo, J. Liu, L. He, M. Du and Z. Zhang, *Small*, 2024, **20**, 2310468.
138 C. Tang, L. Chen, H. Li, L. Li, Y. Jiao, Y. Zheng, H. Xu, K. Davey and S.-Z. Qiao, *J. Am. Chem. Soc.*, 2021, **143**, 7819–7827.
139 H. Xu, S. Zhang, X. Zhang, M. Xu, M. Han, L. R. Zheng, Y. Zhang, G. Wang, H. Zhang and H. Zhao, *Angew. Chem., Int. Ed.*, 2023, **62**, e202314414.
140 L.-Y. Dong, J.-S. Wang, T.-Y. Li, T. Wu, X. Hu, Y.-T. Wu, M.-Y. Zhu, G.-P. Hao and A.-H. Lu, *Angew. Chem., Int. Ed.*, 2024, **63**, e202317660.
141 F. Zhang, Y. Zhu, C. Tang, Y. Chen, B. Qian, Z. Hu, Y.-C. Chang, C.-W. Pao, Q. Lin, S. A. Kazemi, Y. Wang, L. Zhang, X. Zhang and H. Wang, *Adv. Funct. Mater.*, 2022, **32**, 2110224.
142 H. Yang, N. Lu, J. Zhang, R. Wang, S. Tian, M. Wang, Z. Wang, K. Tao, F. Ma and S. Peng, *Carbon Energy*, 2023, **5**, e337.
143 J. H. Kim, D. Shin, J. Lee, D. S. Baek, T. J. Shin, Y.-T. Kim, H. Y. Jeong, J. H. Kwak, H. Kim and S. H. Joo, *ACS Nano*, 2020, **14**, 1990–2001.
144 X. Zhou, Y. Min, C. Zhao, C. Chen, M.-K. Ke, S.-L. Xu, J.-J. Chen, Y. Wu and H.-Q. Yu, *Nat. Commun.*, 2024, **15**, 193.
145 Y. Gu, Y. Tan, H. Tan, Y. Han, D. Cheng, F. Lin, Z. Qian, L. Zeng, S. Zhang, R. Zeng, Y. Liu, H. Guo, M. Luo and S. Guo, *Nat. Synth.*, 2025, **4**, 857.
146 E. Zhang, L. Tao, J. An, J. Zhang, L. Meng, X. Zheng, Y. Wang, N. Li, S. Du, J. Zhang, D. Wang and Y. Li, *Angew. Chem., Int. Ed.*, 2022, **61**, e202117347.
147 J. Gao, H. b Yang, X. Huang, S.-F. Hung, W. Cai, C. Jia, S. Miao, H. M. Chen, X. Yang, Y. Huang, T. Zhang and B. Liu, *Chem*, 2020, **6**, 658–674.
148 J. Du, G. Han, W. Zhang, L. Li, Y. Yan, Y. Shi, X. Zhang, L. Geng, Z. Wang, Y. Xiong, G. Yin and C. Du, *Nat. Commun.*, 2023, **14**, 4766.
149 A. I. M. Albashir, X. Lu, X. Dai and W. Qi, *Commun. Chem.*, 2024, **7**, 111.
150 M. Yang, W. Song, C. Chen, X. Yang, Z. Zhuang, H. Zhang, F. Wang and L. Yu, *Adv. Mater.*, 2025, 2416401, DOI: **10.1002/adma.202416401**.
151 C. Liu, H. Tong, P. Wang, P. Huang, Z. Yang, R. Huang and G. Zhou, *Chem. Eng. J.*, 2023, **476**, 146573.
152 Y. Wang, Y. Zhou, Y. Feng and X. Y. Yu, *Adv. Funct. Mater.*, 2022, **32**, 2110734.

Open Access Article. Published on 21 April 2025. Downloaded on 6/16/2026 6:54:28 AM. This article is licensed under a Creative Commons Attribution-NonCommercial 3.0 Unported Licence.

153 T. C. Nagaiah, D. Schäfer, W. Schuhmann and N. Dimcheva, *Anal. Chem.*, 2013, **85**, 7897–7903.
154 Y. Chang, J. Yang, M. Zhang, M. Yue, W. Wang, J. Li, J. Wang, K. Song, Y. Liu, Y. Zuo and R. Xing, *J. Alloys Compd.*, 2024, **1005**, 176091.
155 R. Gao, L. Pan, Z. Li, C. Shi, Y. Yao, X. Zhang and J.-J. Zou, *Adv. Funct. Mater.*, 2020, **30**, 1910539.
156 Y. Zhang, M. Wang, W. Zhu, M. Fang, M. Ma, F. Liao, H. Yang, T. Cheng, C.-W. Pao, Y.-C. Chang, Z. Hu, Q. Shao, M. Shao and Z. Kang, *Angew. Chem., Int. Ed.*, 2023, **62**, e202218924.
157 H. Li, P. Wen, D. S. Itanze, Z. D. Hood, S. Adhikari, C. Lu, X. Ma, C. Dun, L. Jiang, D. L. Carroll, Y. Qiu and S. M. Geyer, *Nat. Commun.*, 2020, **11**, 3928.
158 R. Shen, W. Chen, Q. Peng, S. Lu, L. Zheng, X. Cao, Y. Wang, W. Zhu, J. Zhang, Z. Zhuang, C. Chen, D. Wang and Y. Li, *Chem*, 2019, **5**, 2099–2110.
159 X.-D. Zhu, Q. Zhang, X. Yang, Y. Wang, J. Wu, J. Gao, J.-J. Zou, G. Wu and Y.-C. Zhang, *SusMat*, 2023, **3**, 334–344.
160 Y. Long, J. Lin, F. Ye, W. Liu, D. Wang, Q. Cheng, R. Paul, D. Cheng, B. Mao, R. Yan, L. Zhao, D. Liu, F. Liu and C. Hu, *Adv. Mater.*, 2023, **35**, 2303905.
161 A. Byeon, J. W. Choi, H. W. Lee, W. C. Yun, W. Zhang, C.-K. Hwang, S. Y. Lee, S. S. Han, J. M. Kim and J. W. Lee, *Appl. Catal., B*, 2023, **329**, 122557.
162 M. Wang, N. Zhang, Y. Feng, Z. Hu, Q. Shao and X. Huang, *Angew. Chem., Int. Ed.*, 2020, **59**, 14373–14377.
163 Y. Wu, Y. Zhao, Q. Yuan, H. Sun, A. Wang, K. Sun, G. I. N. Waterhouse, Z. Wang, J. Wu, J. Jiang and M. Fan, *Nat. Commun.*, 2024, **15**, 10843.
164 L. June Sung, K. Jae Hyung, W. Jinwoo, B. Du San, I. Kyuwook, S. Tae Joo, S. Young Jin and J. Sang Hoon, *Chem*, 2021, **7**, 3114–3130.
165 Y. J. Sa, J. H. Kim and S. H. Joo, *Angew. Chem., Int. Ed.*, 2018, **58**, 1100–1105.
166 K. Dong, J. Liang, Y. Wang, Z. Xu, Q. Liu, Y. Luo, T. Li, L. Li, X. Shi, A. M. Asiri, Q. Li, D. Ma and X. Sun, *Angew. Chem., Int. Ed.*, 2021, **60**, 10583–10587.
167 L. Liu, L. Kang, A. Chutia, J. Feng, M. Michalska, P. Ferrer, D. C. Grinter, G. Held, Y. Tan, F. Zhao, F. Guo, D. G. Hopkinson, C. S. Allen, Y. Hou, J. Gu, I. Papakonstantinou, P. R. Shearing, D. J. L. Brett, I. P. Parkin and G. He, *Angew. Chem., Int. Ed.*, 2023, **62**, e202303525.
168 D. Zhiping and W. Xiaolei, *Nano Res.*, 2022, **15**, 4599–4605.
169 K. H. Koh, A. H. Bagherzadeh Mostaghimi, Q. Chang, Y. J. Kim, S. Siahrostami, T. H. Han and Z. Chen, *EcoMat*, 2023, **5**, e12266.
170 F. She, Z. Guo, F. Liu, Z. Yu, J. Chen, Y. Fan, Y. Lei, Y. Chen, H. Li and L. Wei, *ACS Catal.*, 2024, **14**, 10928–10938.
171 L. Xie, C. Liang, Y. Wu, K. Wang, W. Hou, H. Guo, Z. Wang, Y. M. Lam, Z. Liu and L. Wang, *Small*, 2024, **20**, e2401253.
172 Q. Wu, H. Zou, X. Mao, J. He, Y. Shi, S. Chen, X. Yan, L. Wu, C. Lang, B. Zhang, L. Song, X. Wang, A. Du, Q. Li, Y. Jia, J. Chen and X. Yao, *Nat. Commun.*, 2023, **14**, 6275.
173 P. Chakthranont, S. Nitrathorn, S. Thongratkaew, P. Khemthong, H. Nakajima, R. Supruangnet, T. Butburee, N. Sano and K. Faungnawakij, *ACS Appl. Energy Mater.*, 2021, **4**, 12436–12447.
174 W. Shen, C. Zhang, M. Alomar, Z. Du, Z. Yang, J. Wang, G. Xu, J. Zhang, J. Lv and X. Lu, *Nano Res.*, 2023, **17**, 1217–1224.
175 L. Han, Y. Sun, S. Li, C. Cheng, C. E. Halbig, P. Feicht, J. L. Hübner, P. Strasser and S. Eigler, *ACS Catal.*, 2019, **9**, 1283–1288.
176 C. Zhang, W. Shen, K. Guo, M. Xiong, J. Zhang and X. Lu, *J. Am. Chem. Soc.*, 2023, **145**, 11589–11598.
177 N. Wang, S. Ma, R. Zhang, L. Wang, Y. Wang, L. Yang, J. Li, F. Guan, J. Duan and B. Hou, *Adv. Sci.*, 2023, **10**, 2302446.
178 Y. Liu, S. Liu, J. Jiang, X. Wei, K. Zhao, R. Shen, X. Wang, M. Wei, Y. Wang, H. Pang and B. Li, *Adv. Mater.*, 2025, **37**, 2502197.
179 H. Gong, L. Wei, S. Chen, Z. Chen, T. F. Jaramillo and Z. Bao, *Nano Res.*, 2023, **16**, 11556–11563.
180 K.-H. Wu, D. Wang, X. Lu, X. Zhang, Z. Xie, Y. Liu, B.-J. Su, J.-M. Chen, D.-S. Su, W. Qi and S. Guo, *Chem*, 2020, **6**, 1443–1458.
181 C. Yang, F. Sun, Z. Qu, X. Li, W. Zhou and J. Gao, *ACS Energy Lett.*, 2022, **7**, 4398–4407.
182 J. Shen, Y. Wen, H. Jiang, S. Yu, C. Dong, Y. Fan, B. Liu and C. Li, *J. Phys. Chem. C*, 2022, **126**, 10388–10398.
183 H. Gong, Z. Gong, J. Liu, G. Ye and H. Fei, *Adv. Funct. Mater.*, 2024, **34**, 2316438.
184 W. Liu, R. Chen, Z. Sang, Z. Li, J. Nie, L. Yin, F. Hou and J. Liang, *Adv. Mater.*, 2024, **36**, 2406403.
185 E. A. Moges, C.-Y. Chang, W.-H. Huang, F. T. Angerasa, K. Lakshmanan, T. M. Hagos, H. G. Edao, W. B. Dilebo, C.-W. Pao, M.-C. Tsai, W.-N. Su and B. J. Hwang, *J. Am. Chem. Soc.*, 2023, **12**, 4156–4164.
186 Y. Xia, P. Zhu, Y. Yang, C. Qiu and H. Wang, *ACS Catal.*, 2025, **15**, 4560–4569.
187 J. Wang, J. Li, Z. Li, J. Wu, H. Si, Y. Wu, Z. Guo, X. Wang, F. Liao, H. Huang, M. Shao, Y. Liu and Z. Kang, *Nano Res.*, 2024, **17**, 5956–5964.
188 D. Oh, S. W. Hwang, D. Y. Kim, J. E. Matthews, J. Lee, J. E. A. Acosta, S.-W. Lee, Y. Xu, A. Cho, D. U. Lee, T. F. Jaramillo, D.-H. Seo and J.-W. Jang, *Nat. Synth.*, 2025, **4**, 2698.
189 K. Yu, S. Guan, W. Zhang, W. Zhang, Y. Meng, H. Lin and Q. Gao, *Angew. Chem., Int. Ed.*, 2025, **64**, e202502383.

 This journal is © The Royal Society of Chemistry 2025